

www.acsami.org Research Article

# Improved Electrochemical Performance in an Exfoliated Tetracyanonickelate-Based Metal—Organic Framework

Md Abdul Halim,\* Subrata Karmakar, Md Abdul Hamid, Chironjib Singha Samanta Chandan, Imteaz Rahaman, Michael E. Urena, Ariful Haque, Maggie Yihong Chen, Christopher P. Rhodes, and Gary W. Beall



Cite This: ACS Appl. Mater. Interfaces 2023, 15, 53568-53583



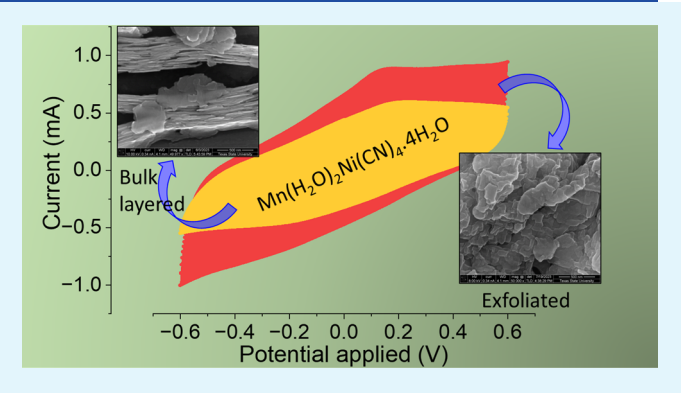
**ACCESS** 

III Metrics & More

Article Recommendations

s Supporting Information

ABSTRACT: Tetracyanonickelate (TCN)-based metal—organic frameworks (MOFs) show great potential in electrochemical applications such as supercapacitors due to their layered morphology and tunable structure. This study reports on improved electrochemical performance of exfoliated manganese tetracyanonickelate (Mn-TCN) nanosheets produced by the heat-assisted liquid-phase exfoliation (LPE) technique. The structural change was confirmed by the Raman frequency shift of the C≡N band from 2177 to 2182 cm<sup>-1</sup> and increased band gap from 3.15 to 4.33 eV in the exfoliated phase. Statistical distribution obtained from atomic force microscopy (AFM) shows that 50% of the nanosheets are single-to-four-layered and have an average lateral size of ~240 nm² and thickness of ~1.2−4.8 nm. High-resolution transmission



electron microscopy (HRTEM) and selected area electron diffraction (SAED) patterns suggest that the material maintains its crystallinity after exfoliation. It exhibits an almost 6-fold improvement in specific capacitance (from 13.0 to 72.5 F  $g^{-1}$ ) measured at a scan rate of 5 mV  $s^{-1}$  in 1 M KOH solution. Galvanostatic charge—discharge (GCD) measurement shows a capacity enhancement from ~18 F  $g^{-1}$  in the bulk phase to ~45 F  $g^{-1}$  in the exfoliated phase at a current density of 1 A  $g^{-1}$ . Bulk crystals exhibit an increasing trend of capacitance retention by ~125% over 1000 charge—discharge cycles attributed to electrochemical exfoliation. Electrochemical impedance spectroscopy (EIS) demonstrates a 5-fold reduction in the total equivalent series resistance (ESR) from 4864  $\Omega$  (bulk) to 1089  $\Omega$  (exfoliated). The enhanced storage capacity in the exfoliated phase results from the combined effect of the electrochemical double-layer charge storage mechanism at the nanosheet—electrolyte interface and the Faradic process characteristic of the pseudocapacitive charge storage behavior.

KEYWORDS: metal—organic framework, tetracyanonickelate, layered structure, liquid-phase exfoliation, surface area, electrochemical performance, pseudocapacitance, Nyquist plot

#### ■ INTRODUCTION

Metal-organic frameworks (MOFs) are a new family of porous materials with well-defined porosities and a large active surface area that are created by mixing metal ions with organic linkers. In addition to the enormous progress in developing new MOF families and their applications in gas storage and separation, catalysis, sensors, and drug delivery, recently, groundbreaking work has been carried out on energy storage systems using MOFs.6 Tetracyanonickelate (TCN)-based MOFs are a novel class of materials composed of metal ions coordinated to organic cyanide (-CN) ligands, forming a three-dimensional porous layered structure. The structural properties of these MOFs are determined by the nature of the metal ions and organic ligands, coordination geometry, and type of metal-ligand bonding. These properties further include the pore size and shape, crystallinity, surface area, and mechanical stability. The structural characteristics of

TCN-based MOFs have a significant impact on their performance as electrochemical storage materials, such as on the capacity for energy storage and the rate of charge and discharge. Understanding these structural properties is crucial for optimizing the performance of these MOFs for electrochemical storage applications. The tetracyanonickelate (II) anions  $[Ni(CN)_4]^{2-}$  serve as the building blocks of the structure. The standard chemical formula is  $T(L)_2Ni(CN)_4$ :  $xH_2O$ , where T is any of the first-row transition metals, L is the

Received: September 20, 2023 Revised: October 25, 2023 Accepted: October 26, 2023 Published: November 9, 2023





pillar, or organic intercalant guest molecule that connects the layers, and x is the quantity of free interstitial water molecules that hydrate and stabilize the structure. The carbon end of the CN ligand is bonded to the Ni<sup>2+</sup> metal centers. The transition metal ion (in this case, T = Mn,  $L = H_2O$ , and x = 4) is bonded to the nitrogen end of the ligands. In a pseudo-octahedral environment, Mn<sup>2+</sup> is connected to four in-plane nitrogen atoms and two water molecules on either side. The structure of TCN-MOF consists of repeating layers of Mn(H<sub>2</sub>O)<sub>2</sub>Ni(CN)<sub>4</sub> with strong covalent bonding within layers and weak van der Waals interaction between layers connected through hydrogenbonded water molecules, which are responsible for their twodimensional (2D) physicochemical properties. In the L<sub>0</sub> phase of  $Mn(H_2O)_2[Ni(CN)_4]\cdot 4H_2O$ , the  $Mn(H_2O)_2[Ni(CN)_4]$ layers acquire an in-phase wave-like configuration due to the alternate linking of their coordinated water molecules by the noncoordinated water molecules,8 which is a fully hydrated structure with four interstitial water molecules (x = 4 in the formula unit). Depending on the quantity of water molecules present, the layers adopt various geometric shapes to reduce the free volume of the interlayer area.

Because of their distinctive layered structure, the twodimensional metal-organic frameworks are suitable for exfoliation, exhibiting major alterations in their chemical and physical characteristics. For example, it has been demonstrated theoretically and empirically that the band structure of MoS<sub>2</sub> can significantly shift when the individual layers of the crystal are isolated. 9,10 Layered double hydroxides (LDH) and structure-engineered hydroxides have both been demonstrated to exhibit a significant level of oxygen evolution reaction (OER) activity. 11 Exfoliation of LDH creates single- or multilayered LDH, which has more active sites and defects and is catalytically more active. 12 An enhanced OER performance was reported in ultrathin metal hydroxides synthesized from square-planar tetracyanonickelate-based MOFs using ultrasonic exfoliation treatment and transformed into metal hydroxide nanosheets with a thickness of about 1.5 nm in aqueous KOH.<sup>13</sup> Significantly, at a current density of 10 mA cm<sup>-2</sup>, the MOL-derived Fe(OH)<sub>3</sub> with an ultrathin layer structure showed increased alkaline oxygen evolution with a low overpotential of 271 mV.<sup>13</sup> Research on how the number of layers and the addition of edges in layered materials affect the photocatalytic effectiveness of hydrogen gas evolution is of critical importance. 14,15 A recent study showed that better charge storage in lithium-ion battery systems 16,17 and supercapacitors<sup>18</sup> can be observed with an increase in the accessible surface area from the bulk crystal to a few or single layers of MoS<sub>2</sub> and ultrahydrophilic graphene stacks.<sup>19</sup> Therefore, it is critically important to control the number of layers, the available reactive sites, and the defects within these layered frameworks to fabricate the next generation of energy conversion and storage devices. The cyanometallate-based MOFs are more appealing than other type of MOFs which involve higher processing costs or complex methods, such as hydrothermal processing, and are chemically intensive, which may, in some cases, require the use of inherently toxic organic chemical entities during the synthetic processes.<sup>20,21</sup> The layered crystal structure of the cyanometallate-based MOFs gives rise to their tunable electrochemical characteristics.<sup>22</sup> There are different studies on cyanometallates being used as electrode materials, which show that they exhibit stable electrochemical behavior in a variety of battery systems, such as metal—air batteries and metal-ion batteries (such as Li-, Na-,

K-, and Al-ion batteries). 23-27 Hexacyanometallate MOFs have recently demonstrated the reversible insertion and extraction of mono- and multivalent ions in both aqueous<sup>28</sup> and nonaqueous electrolytes<sup>29</sup> because of their large interstices, which correspond to the A (alkaline metal ion) sites that can accommodate large-sized ions and water molecules. For example, hexacyanometallate  $KxMFe(CN)_6 \cdot nH_2O$  (M = Ni, Mn, and Co) was tested as the cathode material for calciumion batteries, and the dehydrated KNiFe-MOF with ketjen black (KB) showed reversible capacities of 40 mAh g<sup>-1</sup> even at 12 cycles without destruction of the open framework structure. 30 In order to significantly increase the capacity of their aqueous batteries, Lee et al. employed a vanadium hexacyanoferrate-based MOF as the electrode material.<sup>31</sup> Deng et al. used Co<sub>3</sub>[Co(CN)<sub>6</sub>]<sub>2</sub> in a nonaqueous electrolyte solution as the anode component of K-ion batteries. It was reported that solid-state diffusion-limited potassiation and depotassiation processes are responsible for the high capacity in this framework.<sup>32,33</sup> As an alternative to employing the MOFs directly as electrode materials, Lee et al. explored porous spinel oxides produced from  $Mn_3[Co(CN)_6]_2$  as electrode materials for Zn-air batteries.<sup>34</sup> Most of the electrochemical studies on cyanometallate MOFs involve the use of six-fold octahedral coordination of transition metals in hexacyanometallate as the building blocks, except for the research conducted by Zhang et al., who investigated the electrochemical properties of MOFs built with tetracyanonickelate 4-fold coordination linkers as cathode materials for Li-ion batteries (LIBs).<sup>35</sup>

Some previous studies have reported the electrochemical properties of tetracyanonickelate-based metal-organic frameworks and their derivatives in energy storage devices and catalytic applications. For example, Zhang et al. utilized Fe<sup>2+</sup>Ni(CN)<sub>4</sub>, MnNi(CN)<sub>4</sub>, Fe<sup>3+</sup>Ni(CN)<sub>4</sub>, CuNi(CN)<sub>4</sub>, CoNi-(CN)<sub>4</sub>, ZnNi(CN)<sub>4</sub>, and NiNi(CN)<sub>4</sub> as the cathode materials of Li-ion batteries and reported that the Ni/Fe<sup>2+</sup> system exhibited superior electrochemical properties with a capacity of 137.9 mAh g<sup>-1</sup> at a current density of 100 mA g<sup>-1</sup> compared to the other variants.<sup>35</sup> Through a conformal conversion procedure, a number of metal hydroxide nanosheets were synthesized from metal-organic layers of tetracyanonickelate precursor  $M(H_2O)_2Ni(CN)_4\cdot 4H_2O$  (M = Mn, Fe, Co, and Ni), and their improved OER performance was reported. 13 They have shown that at a low overpotential of 271 mV and a current density of 10 mA cm<sup>-2</sup>, the ultrathin Fe(OH)<sub>3</sub> nanosheets demonstrate an increased alkaline oxygen evolution. Winchester et al. reported that the specific capacitances of the exfoliated MoS2 flakes were an order of magnitude higher than those of the bulk (0.5 and 2 mF cm<sup>-2</sup> for bulk and exfoliated MoS2 electrodes, respectively) while employing a 6 M KOH aqueous solution as an electrolyte.<sup>36</sup> However, utilizing the enormous potential of the tetracyanometalate framework as an electrode material in their exfoliated condition remains unexplored.

In this study, we synthesized a metal—organic framework using the 4-fold coordination of the  $\mathrm{Ni}^{2+}$  in a square-planar environment.  $\mathrm{Mn}^{2+}$  was added as the second transition metal ion into the framework that lies in the pseudo-octahedral lattice position. Bulk crystals of  $\mathrm{Mn}(\mathrm{H_2O})_2[\mathrm{Ni}(\mathrm{CN})_4]\cdot 4\mathrm{H_2O}$  were synthesized and exfoliated through heat-assisted liquid-phase exfoliation technique using 1-dodecyl-2 pyrrolidinone (DDP) as an intercalant. The electrochemical properties of exfoliated TCN-MOF nanosheets were measured as the

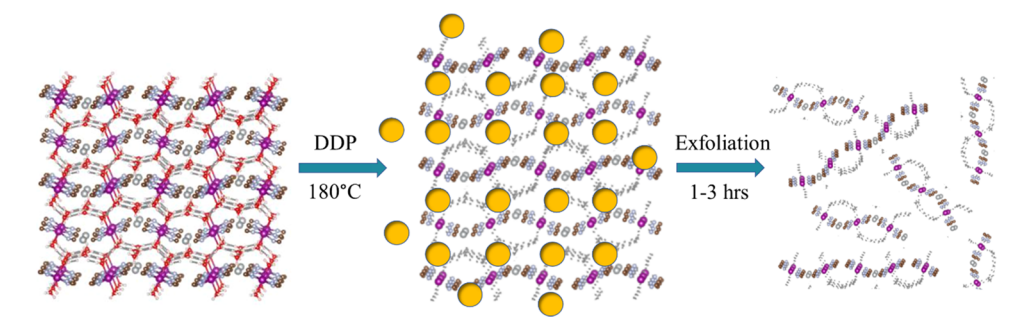


Figure 1. Schematic representation of the exfoliation of TCN-MOF by the heat-assisted liquid-phase exfoliation (LPE) technique.

working electrode (cathode) material in 1 M KOH aqueous electrolyte solution and compared with their bulk counterparts. We anticipate that the results of this study will provide insights into deploying the exfoliated morphology of layered metalorganic frameworks as electrode material in electrochemical applications.

#### EXPERIMENTAL SECTION

Bulk Precursor Synthesis. The bulk layered MOF precursor of manganese tetracyanonickelate Mn(H2O)Ni(CN)4·4H2O were prepared via the bottom-up synthesis approach through the chemical precipitation method reported previously. Few-layered nanoflakes of these MOF precursors were produced by the liquid-phase exfoliation technique described by Nash et al.<sup>37</sup> with slight modification in this work. K<sub>2</sub>[Ni(CN)<sub>4</sub>]xH<sub>2</sub>O and MnCl<sub>2</sub> salts were used to provide the building block anion [Ni(CN)<sub>4</sub>]<sup>2-</sup> and Mn<sup>2+</sup>cation respectively. Trisodium citrate dehydrate (TSCD) was used as a chelating agent to control the reaction rate and growth of crystals. A transparent solution of MnCl2 salt and TSCD was prepared in 100 mL of deionized water at ambient temperature. K<sub>2</sub>[Ni(CN)<sub>4</sub>] was dissolved in 100 mL of water to prepare another clear solution in a different beaker. The two solutions were then combined while being stirred magnetically until precipitates began to form. The resulting mixture was aged at room temperature for 24 h to allow the reaction to finish. The precipitate was separated by centrifugation, and washed multiple times with water and ethanol. Finally, the precipitate was air-dried completely for more than 24 h to remove any excess moisture and collected as a solid powder of precursor crystal.

Liquid-Phase Exfoliation (LPE). In a 10 mL vial, 10 mg of the precursor powder was placed into 1-2 mL of ethanol and allowed to disperse for 5-10 min under continuous magnetic stirring. Once the dispersion became homogeneous, 1-dodecyl-2 pyrrolidinone (DDP) was added at a target concentration ratio of 1.0 mg mL<sup>-1</sup> (w/v), followed by stirring for 10-15 min. The DDP was purchased from Sigma-Aldrich (99%) and used without any further modification. The solution mixture was then placed inside an oven at 180 °C and held for 1 h. The heated mixture was cooled in air for 24 h. When the nanoflakes are separated, drops of the dispersant were taken on glass and Si substrates for further characterization. The excess DDP was removed by heating the substrate in a vacuum oven below 210 °C under a vacuum of 28-29 inHg. Using a Thermo Scientific Multifuge X1R, the mixture was centrifuged at 1000 rpm for 3-5 min and then decanted, yielding a homogeneous suspension. The decantation and centrifugation processes were repeated several times to separate the heavy bulk particles. Although this reduces the total solid concentration of MOF in the solution, it increases the relative percentage of single- or few-layer nanosheets.

Nanosheet Characterization. UV—vis absorbance spectra were measured using a Shimadzu UV-2600 Spectrophotometer in the 220—1400 nm wavelength range at 1 nm scanning intervals. The characteristic nature of cyanometallate was confirmed by the presence of cyano bond (C≡N) vibrational frequencies in the Raman spectra obtained using a Horiba LabRAM HR Evolution spectrophotometer using the 532 nm edge through 1800 grating. The crystallographic

properties of the bulk crystals were determined by wide-angle powder X-ray diffractometry (PXRD) in the Bragg-Brentano (BB) configuration on a Bruker D8 Advance X-ray Diffractometer.<sup>7</sup> The monochromatic Cu K $\alpha$  radiation was utilized with a wavelength of 1.5418 Å, generated by a 40 kV, 25mA source, scanned in the range of  $5-90^{\circ}$  with a step size of  $0.02^{\circ}$  and a scanning rate of  $1.2^{\circ}$  min<sup>-1</sup>. The chemical composition of materials and crystal morphology were analyzed using energy-dispersive X-ray spectroscopy (EDX) and scanning electron microscopy (SEM), which was also reported in our previous study. 7 X-ray photoelectron spectroscopy (XPS) was conducted to analyze the binding energies of the involved elements before and after exfoliation using a ThermoFisher Scientific Nexsa Xray photoelectron spectrometer (XPS). Transmission electron microscopy (TEM) images, both low-magnification and highresolution TEM (HRTEM), and selected area electron diffraction (SAED) patterns were obtained using a Thermo Scientific FEI Talos f200i S/TEM at an operating voltage of 200 kV. TEM samples were prepared by placing nanosheets onto a Formvar film-coated Carbon Type-B, 200 mesh TH, and nickel grid (Ted Pella Inc.). The particles were dispersed in ethanol, pipetted into a small drop on a glass substrate, and collected on the grid by carefully floating the grid (Formvar coating side facing down) onto the drop surface. The surface topography and thickness of the two-dimensional exfoliated nanoflakes were obtained by atomic force microscopy (AFM) in soft tapping mode using a Bruker Dimension ICON AFM. The Brunauer-Emmett-Teller (BET) surface area of the materials was measured by N2 adsorption isotherms for 75 mg of bulk powder and 22 mg of exfoliated sample at 77 K using a Micromeritics ASAP 2020 surface area and porosity analyzer. The samples were degassed at 353 K for 16 h under a vacuum of 100  $\mu$ m Hg.

Electrode Preparation and Electrochemical Measurements. Electrochemical measurements were performed in an aqueous KOH electrolyte solution using a Metrohm Autolab workstation with a twoelectrode parallel-plate configuration. Half-cells were prepared by injecting DDP-dispersed exfoliated nanosheets through a syringe into a battery-grade rectangular nickel foam of  $15 \times 35 \times 1$  mm<sup>3</sup> size, which was used as the working electrode. After the nickel foam was fully soaked with 0.5 mL of nanosheet dispersion ( $\sim$ 0.1 mg cm<sup>-2</sup>), it was then heated at 210 °C under vacuum for 15-20 min to evaporate the excess DDP off the foam. The dried nickel foam was crimped using an automatic Carver Hydraulic Lab Press at 10 000 psi to make sure that the nanosheets do not leave the electrode while it remains dipped into the electrolyte solution. Cyclic voltammetry (CV) measurements were performed at scan rates between 5 and 150 mV s<sup>-1</sup> with a potential window of -0.6 to 0.6 V. Galvanostatic chargedischarge (GCD) and cyclic stability tests were conducted between 1 and 15 A g<sup>-1</sup> current densities. Electrochemical impedance spectroscopy (EIS) was carried out in the frequency range of 0.1 Hz to 100 kHz (KOH) at 10 point frequency steps per decade using a 10 mV RMS ac signal and with no dc bias.

# ■ RESULTS AND DISCUSSION

**Exfoliation of Bulk Crystals into Nanosheets.** Liquidphase exfoliation (LPE) is a method used to exfoliate layered

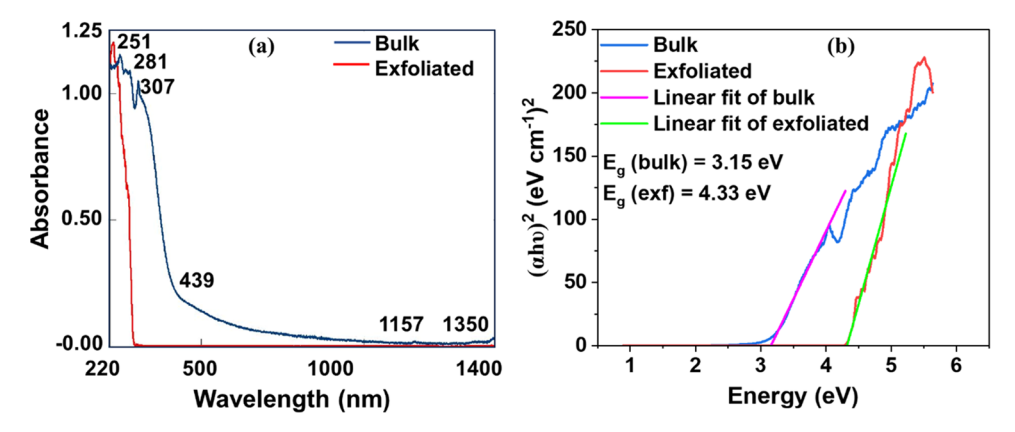


Figure 2. (a) UV-vis absorbance spectra of bulk and exfoliated Mn-TCN MOFs showing characteristic peaks in the near-IR-to-UV wavelength range. (b) Tauc plot with linear extrapolation, giving an indirect band gap of ~3.15 eV for the bulk and a direct band gap of ~4.33 eV for the exfoliated phase.

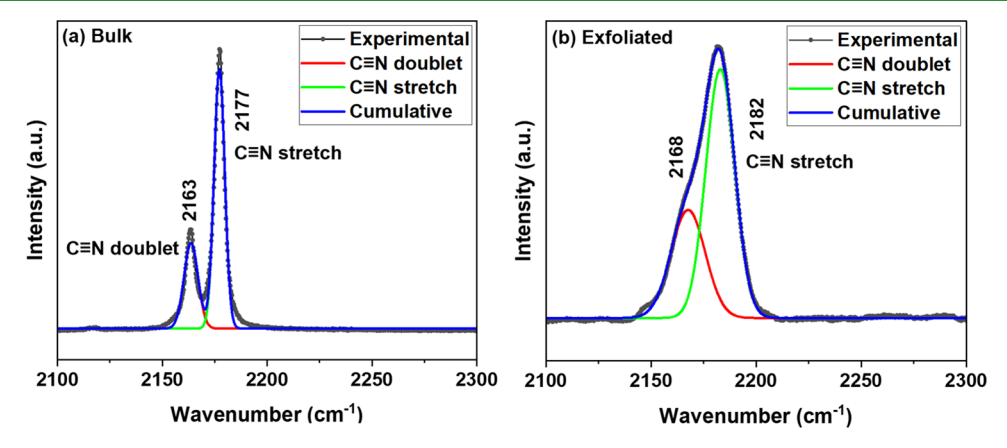


Figure 3. Raman spectra of (a) bulk and (b) exfoliated phases; the doublet peak in bulk crystals almost disappears in the exfoliated few-layered nanosheets with a slight blue shift in the vibrational frequency of the -CN bond.

materials into two-dimensional (2D) nanosheets. It is a versatile and scalable method for producing large quantities of 2D materials with controllable size and thickness and has been used to exfoliate a variety of materials, including graphene, transition metal dichalcogenides, black phosphorus, and metal-organic frameworks. 36,38-40 In LPE, the layered material is dispersed in an intercalant, such as water or an organic solvent, and then subject to a high energy input, such as sonication, to promote the exfoliation process. Different techniques have been reported for exfoliating ultrathin nanosheets of 2D materials, such as mechanical exfoliation, 41 ultrasonic exfoliation,<sup>36</sup> and intercalant-assisted exfoliation.<sup>37</sup> The mechanical process is not suitable for TCN MOF polycrystalline materials, as it has a very low yield of production. The ultrasonic method causes physical damage to the nanosheets; therefore, it is not preferred for this material framework. In this work, heat energy was used instead of sound waves to break the interlayer forces of the material and thus avoid any physical damage to the nanosheets. Figure 1 illustrates the schematic diagram, and Figure S1a-e displays the processing steps used in exfoliating the Mn-TCN MOF and exfoliated MOF nanosheet dispersion.

**UV-Vis Spectroscopy.** Absorbance spectra for T[Ni- $(CN)_4$ ] ·2pyz with T = Mn, Zn, and Cd was reported by Lemus-Santana et al. 42 The existence of colors in this material system was attributed to bright light absorption in the blue spectral region connected to photoinduced charge transfer from metal to ligands. For the diffuse reflectance UV-vis spectroscopy (DRS), samples were illuminated in the ultraviolet-visible wavelength range of 220-1400 nm. In Figure 2a, the charge-transfer bands below 300 nm denote the presence of Ni atom in a square-planar geometry and are attributed to the common building block  $[Ni(CN)_4]^{2-}$ . The broader bands above the 1000 nm range are assigned to spin-allowed  ${}^{3}T_{2g} \leftarrow$ <sup>3</sup>T<sub>A2g</sub>(F) transitions, and other bands in the visible range are attributed to  ${}^{3}T_{1g}(F) \leftarrow {}^{3}TA_{2g}(F)$  and  ${}^{3}T_{1g}(P) \leftarrow {}^{3}TA_{2g}(F)$ transitions of the octahedral metal centers 8,43 Figure 2a compares the absorbance spectra of bulk crystals and exfoliated nanosheets. In this wavelength range, distinct peaks at 1350 and 1157 nm were observed for exfoliated samples in the near-IR region and at 439 nm in the visible range. However, in the absorbance spectrum of bulk crystals, absorption bands are visible only in the UV region associated with the metal-toligand charge transfer (MLCT). In Figure 2b, the Tauc plot of absorbance data shows that the energy band gap is increased from 3.15 eV indirect band for the bulk to 4.33 eV direct band for the exfoliated structure. These results suggest that during exfoliation, the structural integrity of MOF nanosheets is generally preserved while allowing light absorption in the UV region and shows a higher band gap due to the quantum confinement effect of electrons at low dimensions of exfoliated nanosheets.

Raman Spectroscopy. Raman spectroscopy was performed by using a 532 nm laser excitation source. Figure 3a

exhibits the characteristic cyanide (C≡N) peaks in the bulk crystal that appear at 2177 cm<sup>-1</sup> with a doublet peak at 2163 cm<sup>-1</sup> attributed to the allowed  $A_{1g}$  and  $B_{1g}$  vibrations.<sup>42</sup> The significant difference in vibrational frequencies of the bulk and exfoliated morphologies is demonstrated by the Raman C≡N band for exfoliated nanosheets at 2182 cm<sup>-1</sup> in Figure 3b, which does not have a distinguished doublet, unlike its bulk counterpart. It also shows a blue shift in the vibrational energy associated with a reduced number of layers in their exfoliated states. 44 Both the position and shape of the band convey information. The lower band C≡N frequency in bulk crystals might be due to the increased -CN bond length that resulted from the long-range coulombic interaction between many  $Mn(H_2O)_2Ni(CN)_4$  stacked layers. In Figure 3b, the  $-C \equiv N$ band spectrum for the exfoliated phase is deconvoluted using the Gaussian curve fitting, which provides more detailed insights into the underlying structure of the bands. For the fewlayered nanosheet spectrum, the C≡N band is fitted with another underlying band. These bands are characteristics of a few-layered structure as a result of the different interlayer interactions that occur at various depths in the layered framework, whereas the bulk crystals show a strong and sharp doublet peak in the spectrum without any curve fitting.

X-ray Diffractometry (XRD). Using the X-ray diffraction (XRD) technique, the crystal structures of bulk and few-layered TCN were precisely determined. The powdery bulk crystal was measured in the Bragg—Brentano mode, whereas the exfoliated structure was measured in the parallel beam (PB) mode in order to align the incident X-ray beam with the thin film of the sample. As demonstrated in Figure 4, the

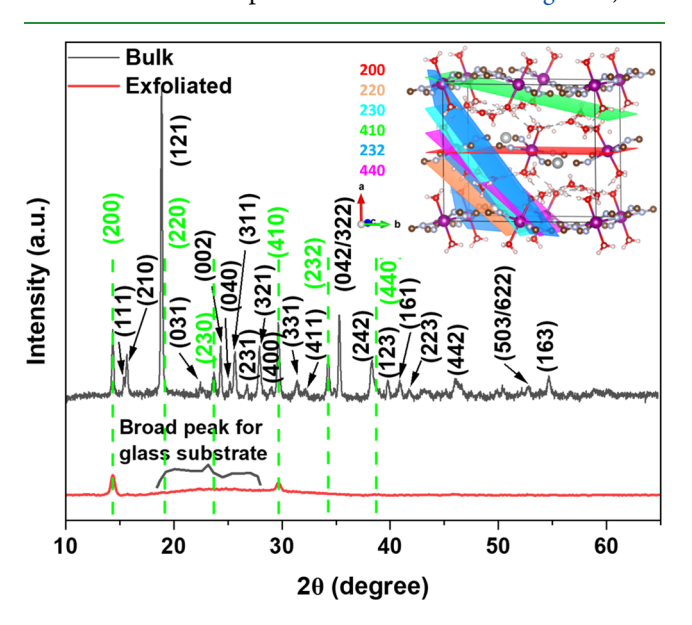


**Figure 4.** X-ray diffraction pattern of bulk crystals and exfoliated Mn-TCN MOF nanosheets (inset picture showing diffraction planes in exfoliated phase).

strongest diffraction peak for the bulk material is observed at  $2\theta = 18.87^{\circ}$  corresponding to the (121) plane, which does not appear in the exfoliated phase due to very low sample thickness. The bulk phase shows a large number of diffraction peaks due to the lower symmetry of orthorhombic crystals, for example, (200)  $\neq$  (020)  $\neq$  (002) because  $a \neq b \neq c$  and so they have different interplanar ( $d_{hkl}$ ) spacings. In the bulk XRD pattern, these peaks are labeled by cross-matching with the

ICDD reference code #01-078-8116 (CCDC# 278583). The most significant among them is the (200) peak at  $2\theta = 14.35^{\circ}$ as the layers are stacked along the a-axis in the bulk crystal and the material exfoliates along the same direction. The intensity of the (200) peak in the exfoliated material diminishes drastically as there are little or no neighboring crystal planes available for constructive interference, indicating that the bulk material was peeled to a few layers. Another characteristic peak in the exfoliated phase is observed at  $2\theta = 29.68^{\circ}$ corresponding to the (410) plane. There are four other crystal planes that can be seen in the corresponding SAED pattern in the TEM image of the exfoliated phase but were not distinctly observed in the XRD pattern due to very low intensity. Peaks after exfoliation are labeled in green for clarity. All exfoliated crystal planes except for (232) are parallel to the c-axis and perpendicular to the direction of exfoliation. The (232) diffraction peak in the exfoliated material is generated from the presence of nanosheets that are not few-layered and have more than 8 or 10 layers. This provides additional information that exfoliation occurs with a reduction in crystal thickness along the a-axis and that the nanosheets mostly remain flat on the substrate. There was no shift recorded in the 2-theta direction, and the intensity of the XRD peaks is very low, which indicates that the exfoliated nanosheets are exceedingly thin. Thus, in few-layered Mn-TCN MOF, the reduction in the XRD peak intensity of the (200) plane is indicative of a fewer number of layers. A broad peak appears between  $2\theta = 17.42$  and  $37.69^{\circ}$  in the exfoliated sample, which is attributed to the diffraction peak of the glass substrate. 45 Powder XRD patterns of both samples are compared in Figure S2a,b.

X-ray Photoelectron Spectroscopy (XPS). The C 1s, N 1s, O 1s, Ni 2p, and Mn 2p XPS spectra of the bulk and exfoliated Mn-TCN MOF are depicted in Figure 5. Lowenergy (500 eV) argon beam etching was performed to remove any atmospheric carbon. To correct the effects of adventitious carbon, a charge correction was applied during the analysis, referencing the binding energy of the C 1s peak to 284.80 eV. The characteristic XPS binding energy peaks for bulk tetracyanonickelate are observed as the Ni-C bond at 282.84 eV, the C bond at 398.74 eV, and the Mn-N bond at 397.01 eV. The survey scan spectrum in Figure 5a confirms the presence of different elements with their corresponding binding energies labeled for the exfoliated structure. Figure 5b-f displays the binding energy shift denoted by the  $(\rightarrow)$ mark for each individual elemental spectrum before and after the exfoliation of the layered crystals. Peaks are labeled for their exfoliated structure. C 1s peaks for both samples are referenced to 284.80 eV (Figure 5b), and the peak shift for Ni-C at  $282.84 \rightarrow 282.53$  eV was calculated. The binding energies involved with the N 1s peak positions for the  $C \equiv N$ bond were found at 398.74  $\rightarrow$  398.76 eV; for Mn-N peaks, the associated binding energies are  $397.01 \rightarrow 396.93$  eV as shown in Figure 5c. The corresponding O 1s peaks for water or organic O appear at 533.08 → 532.77 eV, as depicted in Figure 5d. In Figure 5e, Ni 2p exhibits two recognizable peaks at the binding energies of  $852.72 \rightarrow 853.38$  eV and  $870.33 \rightarrow 871.00$ eV, which were fitted with the two unique doublets (Ni 2p<sub>3/2</sub> and Ni  $2p_{1/2}$ ). In addition, the Mn 2p peaks in Figure 5f having binding energies of  $641.76 \rightarrow 641.17$  eV and  $653.81 \rightarrow 653.28$ eV in the spectra of divalent manganese ions (Mn<sup>2+</sup>) are attributed to the Mn  $2p_{3/2}$  and Mn  $2p_{1/2}$  orbitals respectively, further validating the fact that the exfoliated nanosheets are likewise produced from the Mn variant of the tetracyanonick-

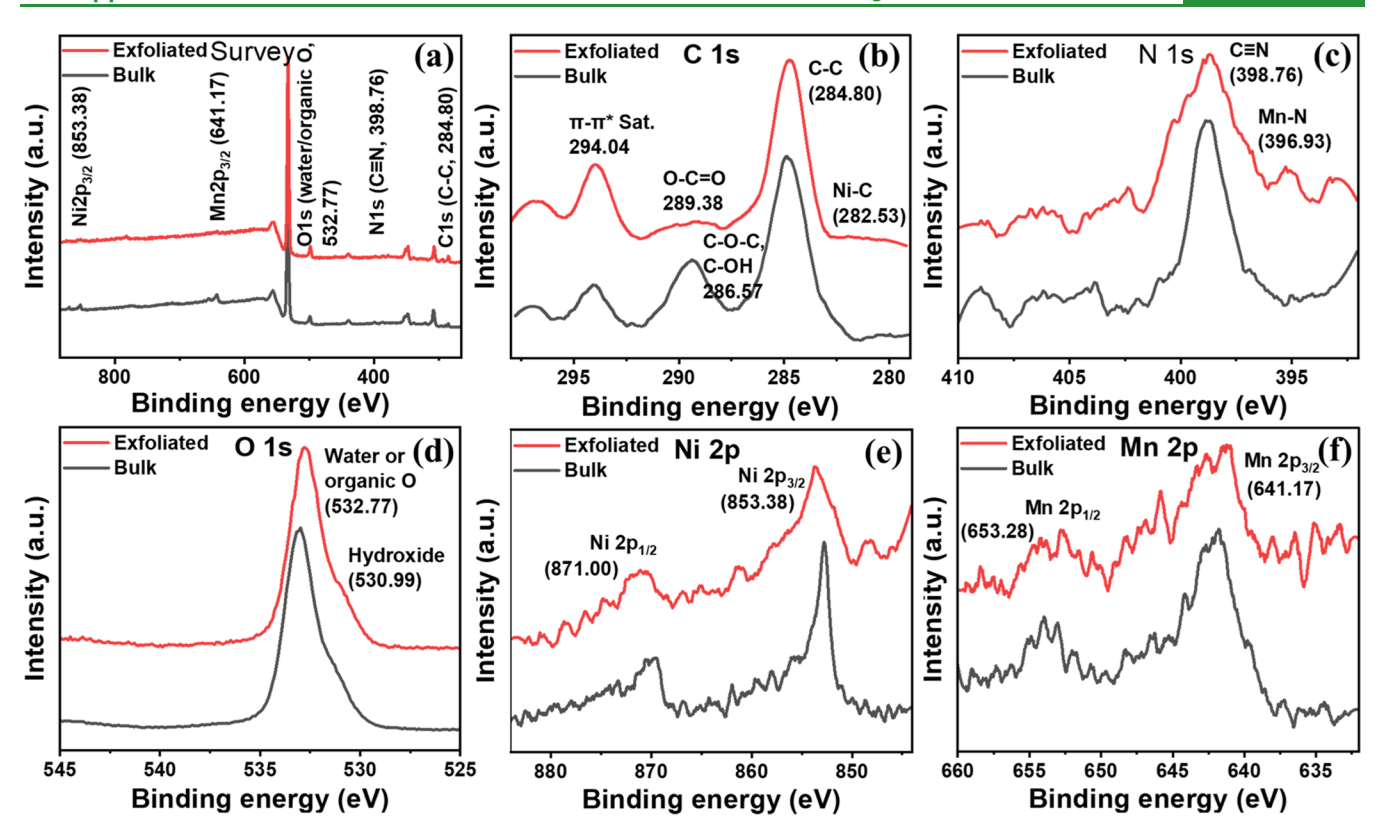


Figure 5. XPS spectra of Mn-TCN MOF: (a) survey scan, (b) C 1s, (c) N 1s, (d) O 1s, (e) Ni 2p, and (f) Mn 2p spectra of bulk crystals and exfoliated nanosheets.

elate framework. The slight shifts in the binding energies can be attributed to the change in the material thickness in their exfoliated phase. In a two-dimensional configuration, the single- or few-layered thicknesses may cause quantum confinement of the electronic density of states, which influences charge distribution within the material, leading to a shift in the XPS binding energy. Because of exfoliation, new surface sites in the nanosheets may be introduced into functional groups  $(SO_4^{2-}, OH^-, C=O)$  from the solvent used, altering the chemical environment. This modification can affect the binding energies in XPS due to changes in the electronegativity or bonding states. The deconvoluted C 1s, N 1s, O 1s, Ni 2p, and Mn 2p spectra are systematically compared in Figures S3–S7.

Scanning Electron Microscopy (SEM). The bulk crystal and exfoliated nanosheet morphologies were revealed using scanning electron microscopy (SEM). Figure 6a depicts the layered nature of bulk crystals with a thickness of ~500 nm. In Figure 6b, the layered crystals are exfoliated into nanosheets with their lateral dimension measured in the range of 20-200 nm. Some of these nanosheets form clusters and sit on top of each other due to their high electrostatic surface charge and cause reaggregation of exfoliated sheets. The DDP used as the exfoliant also provides stabilization of the nanosheet dispersion. It is adsorbed onto the nanoparticle surfaces, creating a protective layer of hydrophobic tails that face outward. This hydrophobic layer creates a repulsive barrier between nanoparticles, preventing them from coming into direct contact and forming aggregates. The energy-dispersive X-ray (EDX) elemental mapping in Figure 6c displays uniformly distributed elements over the exfoliated nanosheets.

The EDX elemental mapping for the bulk crystal is shown in Figure S8.

Atomic Force Microscopy (AFM). The surface topography and thickness were measured by using atomic force microscopy (AFM). Figure 7a-f displays the typical soft tapping-mode AFM images of the bulk crystal and exfoliated nanosheets that were drop-cast onto glass and Si substrates. The AFM data for the exfoliated phase were collected using different scan sizes such as 300 nm, 500 nm, and 1 µm. The monolayer nanosheets were visible at ~300 nm scan size. Gwyddion software was used to analyze the scans and extract the thickness profile by drawing arbitrary lines passing over several nanosheets. This process was repeated multiple times. The data were exported and further plotted using Origin software. Before exfoliation, the bulk material has thousands of stacked layers forming hexagonal crystals with thicknesses between 0.7 and 2.8 µm. Figure 7c depicts the fractional distribution of the number of layers in multiple of thousands associated with bulk crystals. Upon exfoliation, the layers become separate and form single- or few-layered nanosheets. A single layer (monolayer) of this material comprises a unit cell that has three interconnected sublayers of Mn(H2O)Ni(CN)4 in which the average measured thickness of such a single layer is about 1.2 nm. A range of sheet thickness from ~1.226 to 12.284 nm was obtained for the exfoliated nanosheets. This variation in sheet thickness is related to the presence of singlelayer or few-layer nanosheets. For example, the thickness of single-layer nanosheets is ~1.2 nm and that of four- or fivelayer nanosheets corresponds to a typical topographic height of  $\sim$ 4.8–6.0 nm. The nanosheets may laterally combine hundreds of individual nanoflakes with an average length of 20 nm and width of 12 nm. The statistical distribution of exfoliated

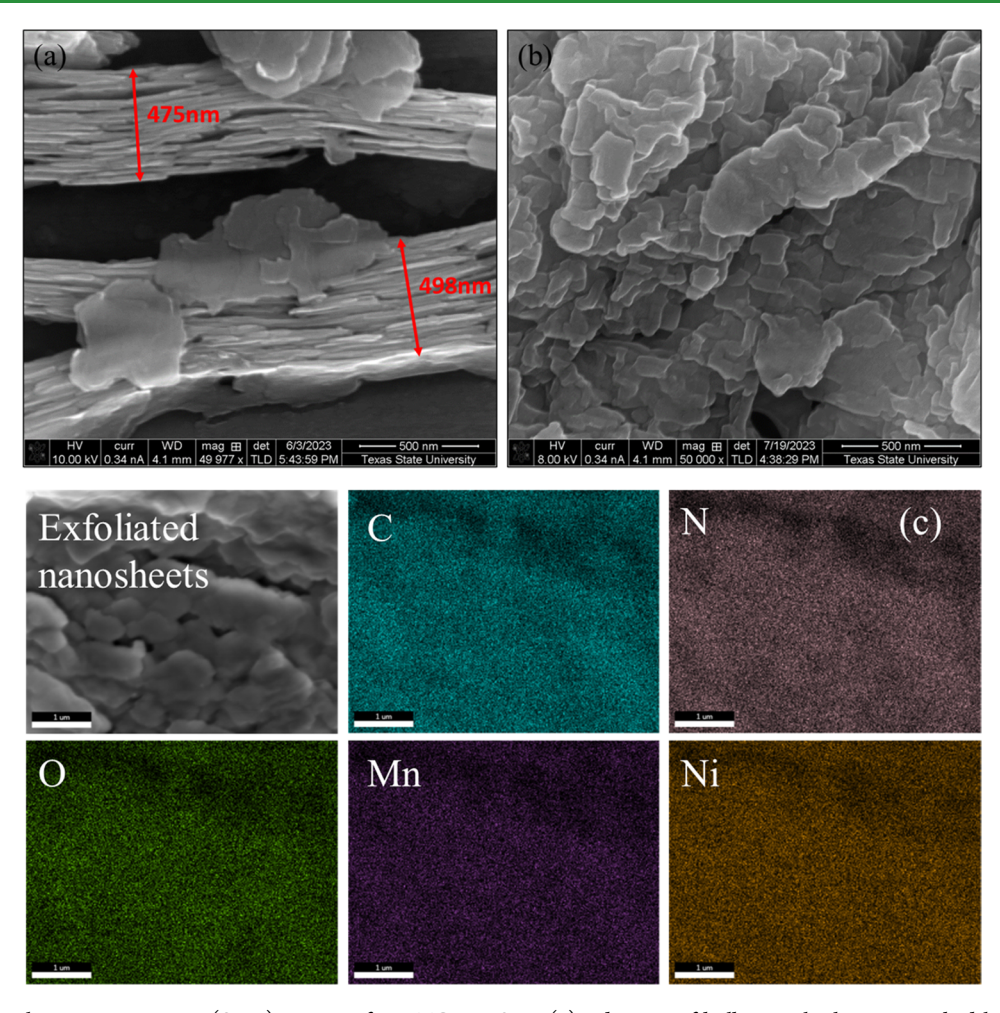


Figure 6. Scanning electron microscopy (SEM) images of Mn-TCN MOFs: (a) side view of bulk crystals showing stacked layers, (b) exfoliated few-layered nanosheets, and (c) EDX elemental mapping of nanosheets.

nanosheets is shown in Figure 7f. AFM statistics show that 25–30% of the thin nanosheets (excluding the unexfoliated particles) were made up of single-layers, and a cumulative 50–60% of the nanosheets had four to six layers. Figure S9 displays additional AFM images with the height profiles.

Transmission Electron Microscopy (TEM). The manganese tetracyanonickelate (Mn-TCN) nanosheet morphology was revealed by transmission electron microscopy (TEM). The exfoliated morphology of single- and few-layer nanosheets is presented in Figure 8. A nanoflake is visible with multiple layers in Figure 8a,b, which shows that many of these nanoflakes constitute few-layer nanosheets. Figure 9 displays TEM images of Mn-TCN for both bulk crystals and exfoliated nanosheets. The low-magnification image in Figure 9a shows overlapped crystal flakes sitting on top of one another and forming a cluster of particles. In contrast, as shown in Figure 9d, the 3D flakes turned into two-dimensional single- or fewlayer dispersed nanosheets upon exfoliation with lateral sizes between 200 and 300 nm (Figures S10 and S11 present more TEM images). The characteristic nanosheet morphology of the exfoliated phase can be observed from the transparent contrast between the overlapping nanoflakes. High-resolution TEM (HRTEM) images were analyzed to further examine the crystal structure of the samples. In Figure 9b, the HRTEM image shows that bulk crystals have multiple stacked layers, as indicated by the arrow marks. The exfoliated nanosheets

composed of single layers or two layers are confirmed by the HRTEM images in Figure 9e. The selected area electron diffraction (SAED) patterns of the bulk crystal and exfoliated nanosheets are shown in Figure 9c,f, respectively. For the bulk crystal sample, the SAED image forms the typical ring pattern of a layered structure (Figure 9c). This corresponds to the presence of many underlying layers in the bulk crystal in which electron diffraction occurs from all possible crystal planes with different angular orientation in the highly assymetric orthorhombic crystal, therefore forming a continuous ring structure. Exfoliated nanosheets, on the other hand, have a single-layer, a bilayer, or a few layers in which stacked layers are more likely to have one angle of orientation or a very low angular twist relative to one another. In such a case, electrons get diffracted from one or a few adjacent layers, which reflect the crystallographic atomic positions with great clarity in Figure 9f. Figure S12 describes how the SAED pattern is indexed for the corresponding crystal planes. Using the SAED pattern, the interplanar spacings were calculated for  $d_{400}$  = 0.306 nm and  $d_{440} = 0.232$  nm, corresponding to the (400) and (440) crystal planes in the bulk and exfoliated phases, respectively. The SAED pattern for the bulk sample was also labeled for the different zone axes, as depicted in Figure 9c. In Figure 9e,f, the HRTEM image and SAED pattern clearly indicate that the exfoliated nanosheets retained the crystallinity

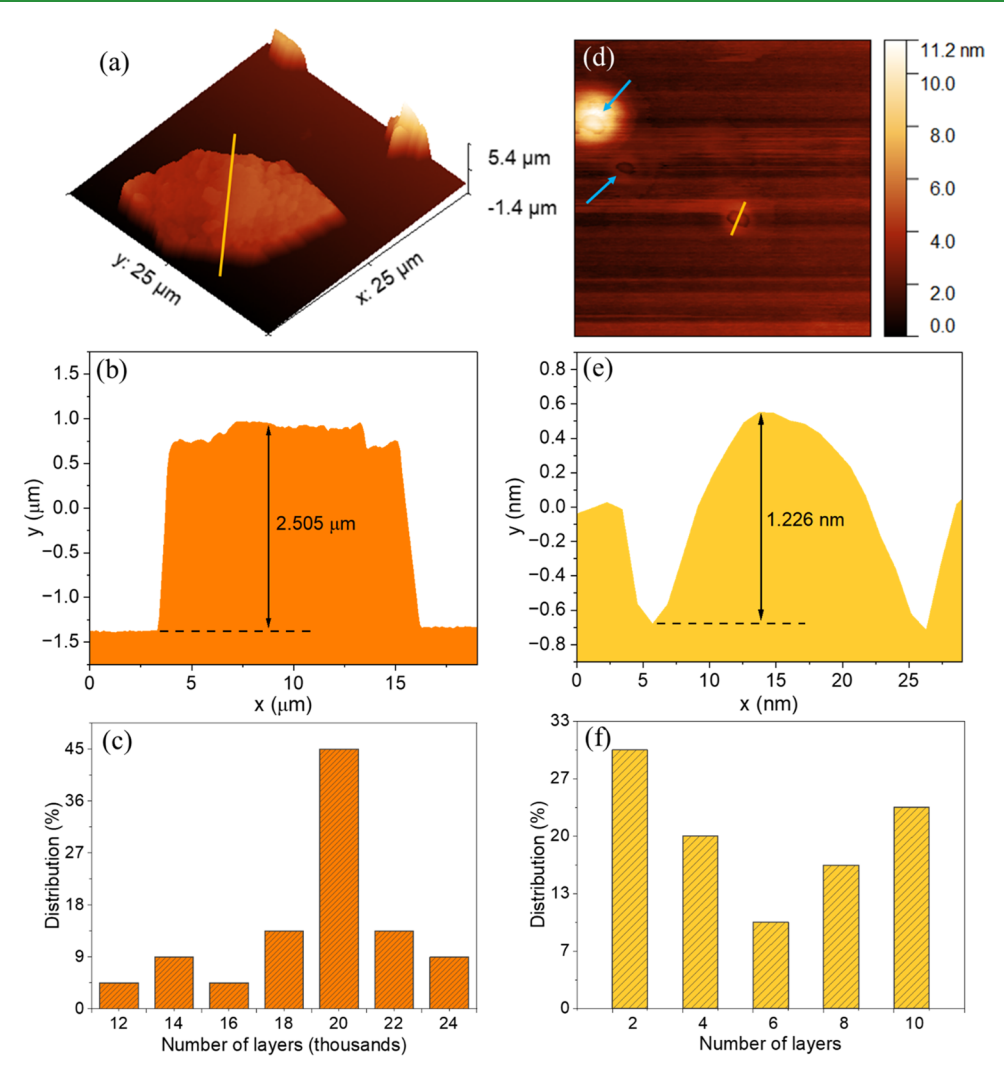


Figure 7. (a, d) AFM images of Mn-TCN MOF bulk and exfoliated nanosheets. (b, e) Corresponding height profiles obtained along the lines indicated in the AFM images. (c, f) Layers and thickness distribution histograms of bulk and nanosheets, as estimated from the AFM analysis.

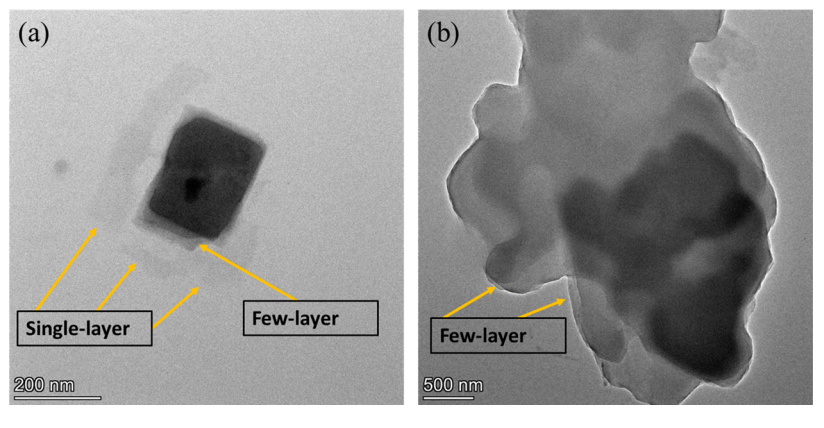


Figure 8. TEM images of exfoliated Mn-TCN MOF: (a) nanoflake and (b) few-layered nanosheets.

of the material, and their original  $L_0$  phase orthorhombic structure was not altered during the exfoliation process.

**Brunauer–Emmett–Teller (BET) Measurement.** The pore size and Brunauer–Emmett–Teller (BET) surface area were confirmed by the  $N_2$  adsorption–desorption isotherms for bulk and exfoliated samples. Figure 10 shows a BET surface area of 0.6935 m<sup>2</sup> g<sup>-1</sup> for the bulk crystal and 8.6588 m<sup>2</sup> g<sup>-1</sup> for the exfoliated phase, demonstrating up to an order of

magnitude increase in the surface area. However, upon exfoliation, the pore size of the frameworks was reduced from an average adsorption pore width of 1020.660 to 476.440 Å. In their bulk phase, the crystals form a 3D network of – NC–Ni–CN–, which produces a very rigid porous channel throughout the structure. The reduction in pore size might be due to the collapse of the rigid pores as the layers disintegrate into flat sheets upon exfoliation, causing the destruction of the

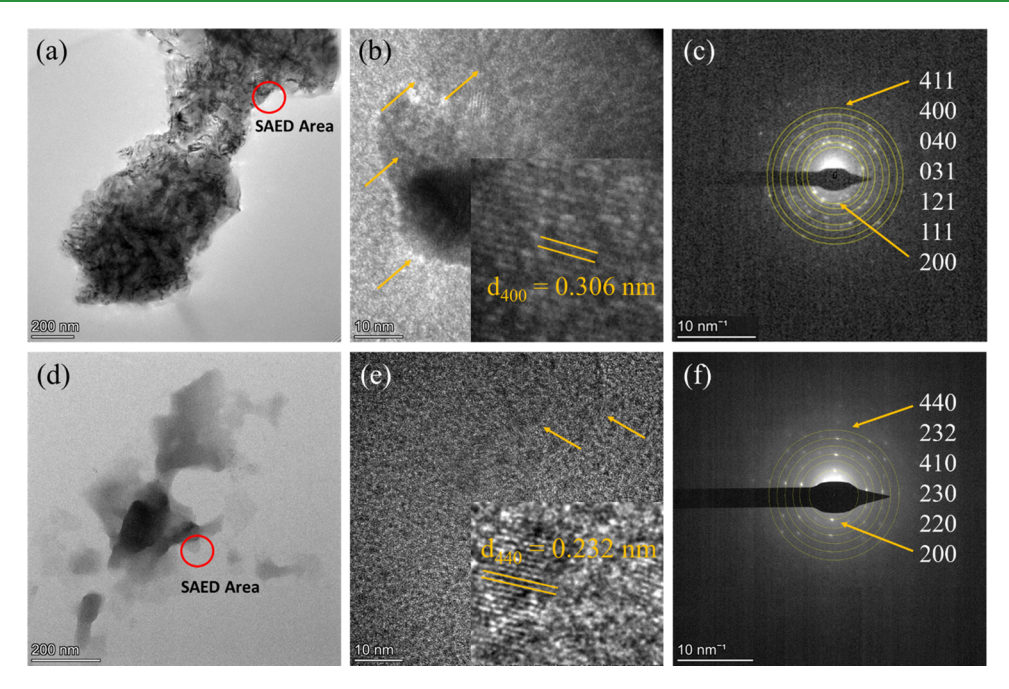


Figure 9. Transmission electron microscopy of Mn-TCN MOFs: (a, d) Low-magnification TEM image, (b, e) HRTEM image, and (c, f) SAED pattern of bulk crystal and the exfoliated nanosheet.

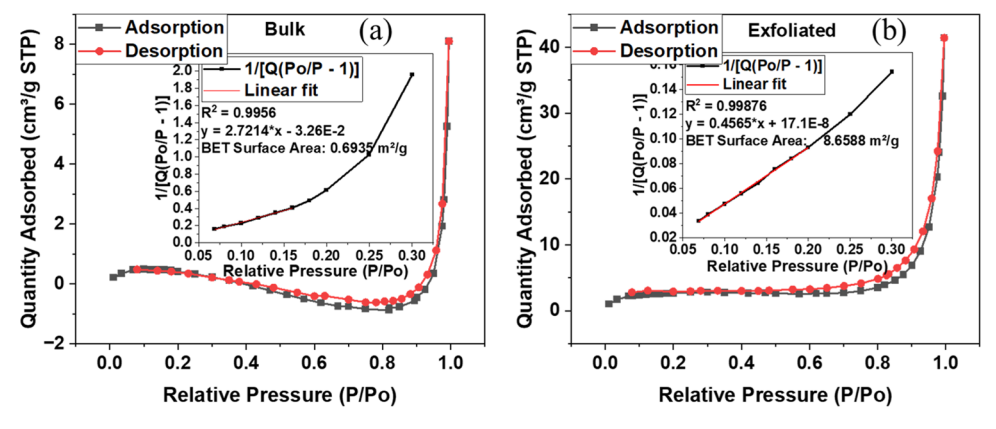


Figure 10. N2 adsorption—desorption isotherms of the (a) bulk and (b) exfoliated phases of the Mn-TCN MOF.

3D porous network. Therefore, although the BET surface area increases upon exfoliation, the average pore size decreases as a result of the change in particle morphology.

Cyclic Voltammetry (CV) Test. The electrochemical cell was set up by constructing two electrodes in a parallel-plate configuration, as is commonly used in real-world devices without any binders or additives. Two different samples, herein referred to as bulk crystals and exfoliated nanosheets, were crimped into the nickel foam to build a working electrode with a constant geometric area of 5.25 cm<sup>2</sup>. The electrochemical behavior was characterized by cyclic voltammetry (CV) and electrochemical impedance spectroscopy (EIS) in a 1 M KOH electrolyte solution. The electrical connection of the working electrode with the external circuit was made by using a thin copper strip (Figure 11a). A high-purity platinum wire was used as the reference electrode. The experiment was conducted at ambient temperature and pressure. In Figure 11b,c, the CV measurements show excellent responses, having nearly rectangular curves with redox peaks for both samples, which are typical of the pseudocapacitance (PC).46,47 The PC charging current is related to the surface area of the electrode,

as well as the redox charge storage processes that occur at the electrolyte-electrode interface. A significant difference in the specific capacitance between the bulk crystals and exfoliated nanosheets was observed, with the exfoliated nanosheets showing almost six times higher specific capacitance than the bulk crystals. This is expected because the PC charge is most noticeable in systems with a high surface area-to-volume ratio, such as in materials with pores or structures in the size range of micrometers to nanometers.<sup>48</sup> The increase in the specific capacitance of ~6 times for the exfoliated nanosheets is less than the  $\sim 13$  times increase in the surface area, which is consistent with a charge storage mechanism that involves both electrochemical double-layer capacitance at the electrodeelectrolyte interface and a faradic process (as observed by the redox peaks in the CV curves in Figure 11b,c) that involves charge storage at the surface and below the surface. The bulk crystal sample has a three-dimensional layered structure with intrinsic porosity and an average thickness of 2.5 µm, which was exfoliated into two-dimensional single- to few-layered nanosheets with an average thickness of  $\sim$ 1.2–4.8 nm through the liquid-phase exfoliation technique. This transformation

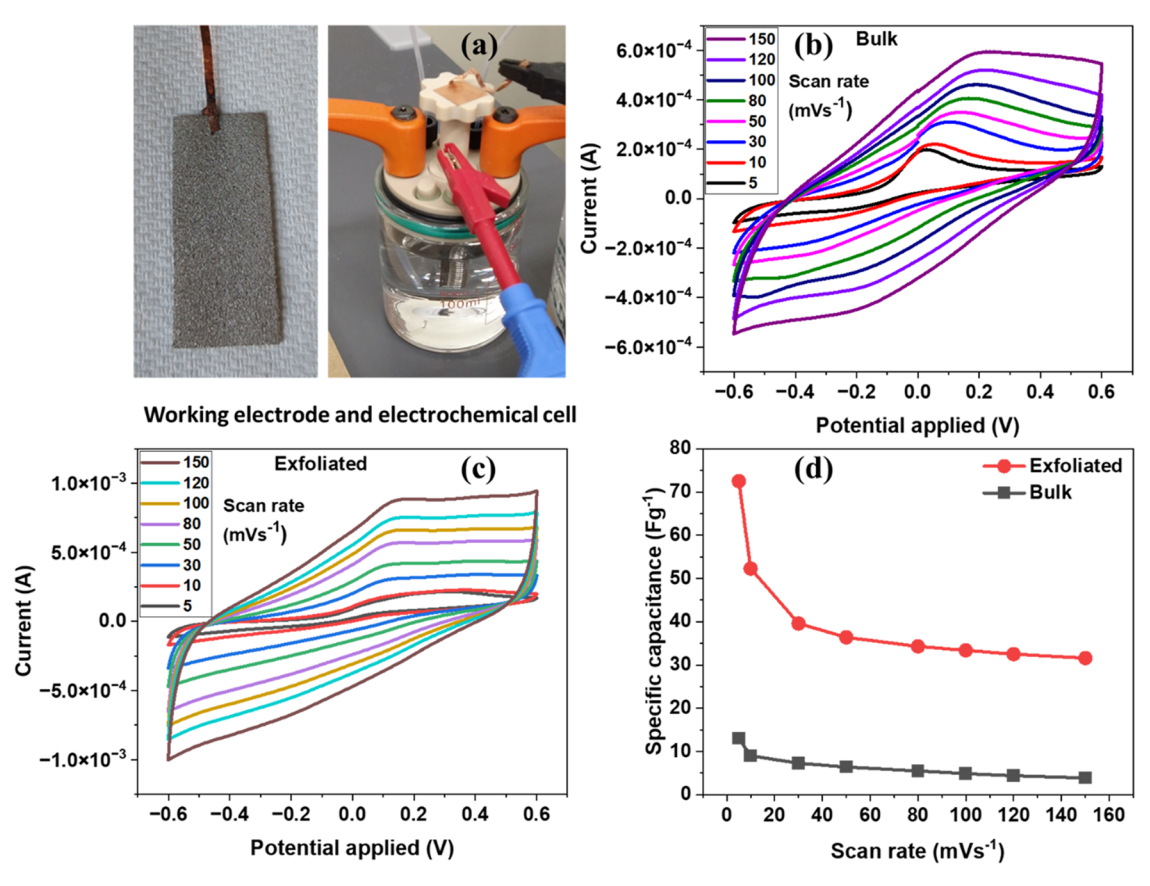


Figure 11. (a) Electrode configuration and experimental setup used for electrochemical characterization of Mn-TCN MOFs. (b) Cyclic voltammetry at various scan rates of bulk crystals using 1 M KOH electrolyte. (c) Cyclic voltammetry at various scan rates of nanosheets. (d) Variation of specific capacitance (F g<sup>-1</sup>) with scan rates (mV s<sup>-1</sup>).

greatly enhanced the specific surface area of the material. The variation of specific capacitance with scan rates is displayed for samples before and after exfoliation in Figure 11d, which demonstrates that the exfoliated sample has higher capacitance and hence a larger electroactive surface area. 49,50 The CV measurement was also performed in the non-faradic region at a 0.45V potential window (Figures S13 and S14). A slight difference in the area under the CV curve for bulk and exfoliated phases is observed when compared with the nonfaradic region. However, the effect of exfoliation is more significant when a wider potential window of -0.6 to +0.6 V is applied.

Capacitance values were obtained from the CV curves using the following formula<sup>36</sup>

$$C_{\rm sp} = \frac{\int i \, \mathrm{d}V}{\mathrm{sm}\Delta V} \tag{1}$$

The integral  $\int i dV$  represents the area under the CV curve, s is the scan rate, m is the mass of the material used in a single electrode exposed to the electrolyte, and  $\Delta V$  is the potential window for scanning. The highest capacitance value obtained as PC electrodes for the exfoliated phase at a scan rate of 5 mV s<sup>-1</sup> is 72.5 F g<sup>-1</sup>, almost 6 times the value obtained using bulk crystals, which is 13.0 F g<sup>-1</sup>. The increase in capacitance is consistent with the increased specific surface area of Mn-TCN due to exfoliation. This increase was confirmed by measuring the BET surface area of the bulk and exfoliated samples by using the  $N_2$  adsorption—desorption isotherms (Figure 10).

Galvanostatic Charge-Discharge (GCD) Test. Galvanostatic charge-discharge (GCD) experiments were performed at current densities of 1, 3, 5, 7, 10, 12, and 15 A g<sup>-1</sup> to examine the rate capability of the bulk and exfoliated Mn-TCN electrodes. Figure 12a,b shows the GCD curves for both phases at different current densities. The exfoliated electrode exhibits longer charge and discharge times than its bulk counterpart due to its higher active surface area, which allows increased ion adsorption. Based on the discharge section of the GCD curves, the gravimetric specific capacitance ( $C_{o}$ , F g<sup>-1</sup>) was also calculated using eq 2.

$$C_{\rm g} = \frac{I/m}{\Delta V/\Delta t} \tag{2}$$

where I is the discharge current (A), m is the mass of active material (g),  $\Delta V$  is the potential drop during the discharge cycle (V), and  $\Delta t$  is the discharge time (s).

The rate performances are displayed in Figure 12c at different current densities. In comparison to the bulk, the GCD curve of the exfoliated electrode shows a high specific capacitance of  $\sim$ 45 F g $^{-1}$  at 1 A g $^{-1}$  current density. Notably, the exfoliated phase demonstrates a high capacitance retention of 56% at 15 A  $g^{-1}$ . The open-circuit potential (OCP) was also measured (Figure S15) to investigate the equilibrium state of the system and the stability of the electrode. OCP was performed by measuring the voltage difference between the electrode and its surrounding electrolyte solution without applying any external current for 3600 s. The OCP for the exfoliated sample was found to be larger than that of the bulk

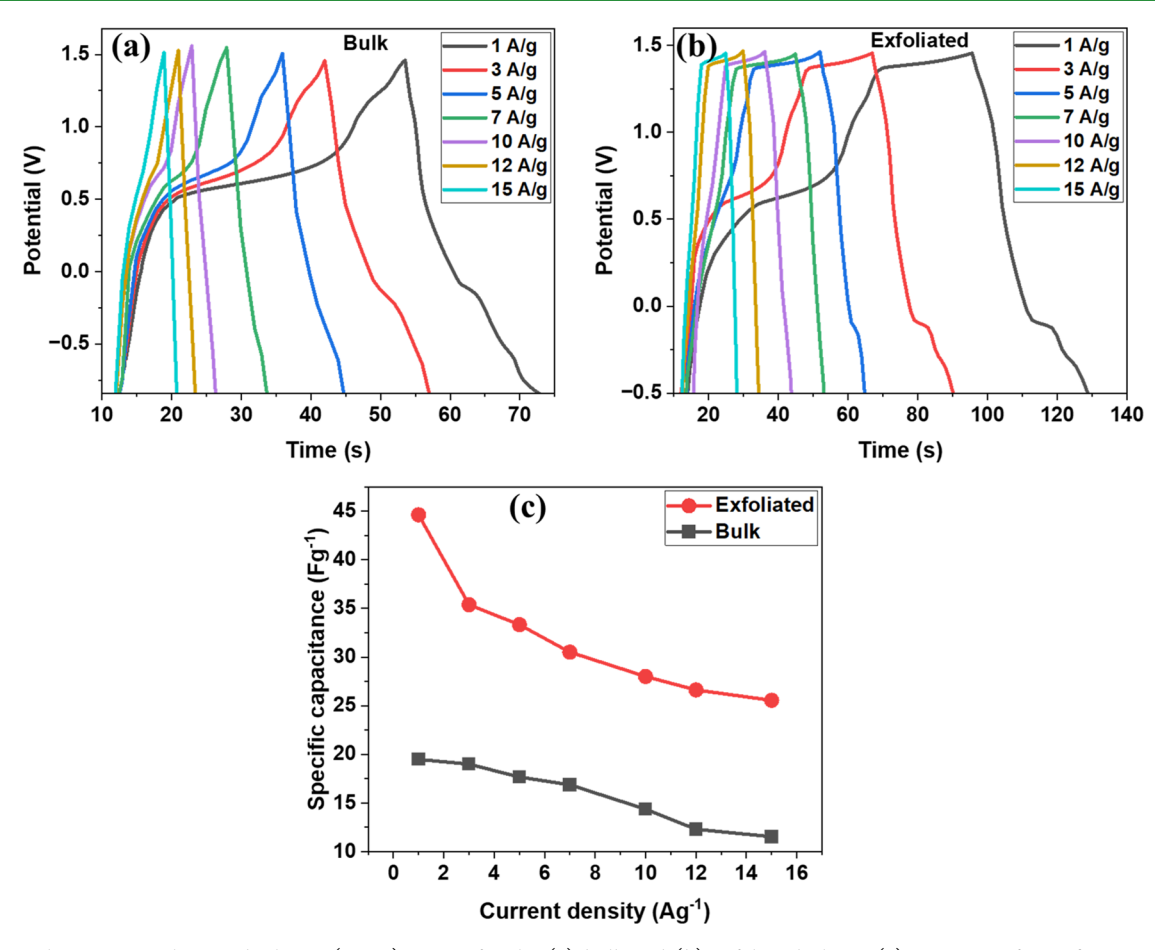


Figure 12. Galvanometric charge—discharge (GCD) curves for the (a) bulk and (b) exfoliated phase; (c) variation of specific capacitance with increasing current density.

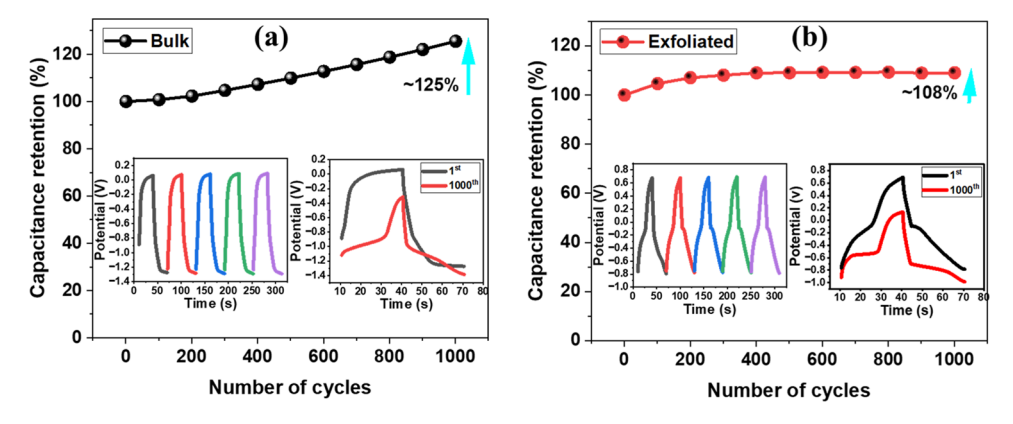


Figure 13. Capacitance retention curves for the (a) bulk and (b) exfoliated phases; inset: (left) the first 5 cycles and (right) comparison between the 1st and 1000th of cyclic stability tests.

phase, and a dynamic behavior was observed for the exfoliated phase as it shows a sudden increase in OCP at 1575s, which later becomes stable for the rest of the testing period. This change may be associated with various electrochemical processes such as adsorption/desorption of species on the electrode surface and alterations in the local environment.<sup>51</sup>

**Cyclic Stability Test.** The long-term cyclic stability test was conducted at a constant current density of 1 A  $\rm g^{-1}$  for both bulk and exfoliated electrodes over 1000 cycles. Capacitance retention is a critical parameter in assessing the long-term performance and stability of energy storage devices. This was calculated using the following formula

capacitance retention (%): 
$$C_{\text{ret}} = \frac{C_{\text{f}}}{C_{\text{i}}} \times 100$$

where  $C_i$  and  $C_f$  are the initial and final capacitance values measured before and after 1000 charge—discharge cycles, respectively.

Figure 13a shows a gradual increase in the capacitance for the bulk phase, resulting in an increase in the capacitance retention up to 125% over 1000 charge—discharge cycles. A similar phenomenon has been described in the literature for other 2D layered material systems such as MoS<sub>2</sub> and explained by the activation of the surface area through electrolyte ion

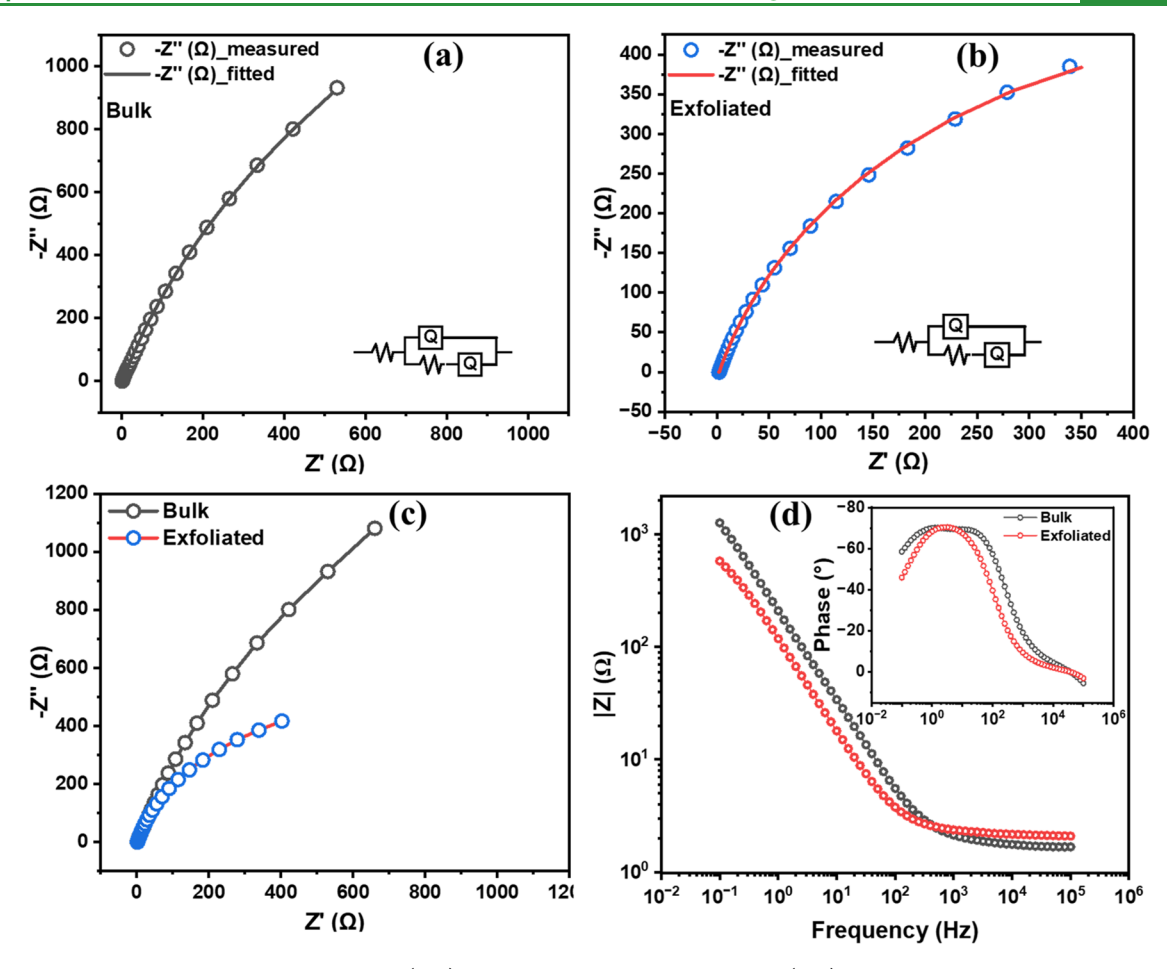


Figure 14. Electrochemical impedance spectroscopy (EIS) measurement of Mn-TCN MOFs: (a, b) Nyquist plots, where the solid lines represent the best fit to the modified Randles equivalent circuit model, show the real component of impedance, Z', against the imaginary component of impedance, Z''; (c) comparison of the Nyquist plot between the bulk and exfoliated phases. (d) Bode plot comparison, presenting the modulus of the impedance, |Z|, and phase angle (inset) against the frequency.

diffusion into the interlayers of MoS<sub>2</sub>. The charge-discharge process drives the electrolyte ions to enter the interlayer regions of the bulk material and eventually causes it to be exfoliated through an ion insertion technique. This leads to an increase in the electrochemically active surface area of the bulk phase, which is reflected in their increasing capacitance retention with the number of cycles. The increase in capacitance as a result of ion intercalation and partial exfoliation was also reported by Bissett et al.<sup>53</sup> The increasing trend for bulk Mn-TCN remains even after 1000 chargedischarge cycles. However, for the exfoliated phase, although the capacitance retention increases in the beginning up to a few hundred cycles, it shows an almost flat curve after 400 cycles, suggesting no further increase in the storage capacity, Figure 13b. This distinct behavior of the bulk and exfoliated phase might be attributed to the fact that, in the bulk material, the layers continue to become exfoliated with repeated charge and discharge, but the exfoliated phase, which is already delaminated into single or few layers, undergoes further exfoliation only partially until 300-400 cycles, and no further exfoliation occurs after that. A cyclic stability test beyond 1000 cycles would reveal the maximum capacity retention for the bulk material and any fluctuation in the observed steady curve for the exfoliated phase.

Electrochemical Impedance Spectroscopy (EIS). Electrochemical impedance spectroscopy (EIS) was performed to

analyze these samples further. With a 10 mV RMS voltage and no dc bias, the impedance spectra of the KOH device were recorded over the frequency (*f*) range of 100 kHz to 100 MHz. In Figure 14, a comparison of the impedance spectra for each of the electrodes is presented in Nyquist plots (Figure 14a-c) and Bode plots (Figure 14d). The Bode plots demonstrate that in the KOH electrolyte solution, the impedance significantly decreased as the electrode was changed from bulk crystal to one with exfoliated nanosheets. Because of the increased double-layer capacitance, the exfoliated sample had a somewhat lower impedance amplitude than the bulk sample. The Nyquist plot of the real and imaginary parts of the impedance is represented in Figure 14a,b. This gives a direct estimate of the equivalent series resistance (ESR) of the device. 54,55 For instance, with the KOH-based system, the high-frequency intercept of the real axis was used by Winchester et al. as an approximation of the ESR value for exfoliated MoS2 nanosheets.<sup>36</sup> The impedance spectrum can be fitted to an equivalent circuit to achieve a deeper understanding. A suitable circuit can provide an overview of the physical processes that may be taking place in the system. 54,56 In Figure 14a,b, the impedance spectra were fitted to the Randles equivalent circuit,<sup>57</sup> which models the electrochemical impedance of this system. It consists of a resistor  $(R_s)$ , representing the solution resistance, in series with a constant phase element (CPE) and the Warburg impedance  $(Z_W)^{58-60}$  which account for the

Table 1. Impedance Spectra Fitting Parameters from the Nyquist Plot

sample (1 M KOH)	$R_{\rm s} \; (\Omega)$	$CPE_1$ (F)	$n_1$	CPE <sub>2</sub> (F)	$n_2$	$R_{ m ct} \ (\Omega)$	goodness of fit	capacitance total fitted (F)	capacitance experimental (F)
bulk	1.733	$9.849 \times 10^{-4}$	0.8243	$0.7048 \times 10^{-4}$	0.5436	4864	$1.301 \times 10^{-3}$	$10.5538 \times 10^{-4}$	$8.64 \times 10^{-4}$
exfoliated	2.182	$17.99 \times 10^{-4}$	0.8353	$1.131 \times 10^{-9}$	0.8595	1089	$6.882 \times 10^{-4}$	$17.99 \times 10^{-4}$	$19.93 \times 10^{-4}$

Table 2. Capacitive Performance of Various Similar MOFs

material system	surface area $(m^2 \ g^{-1})$	scan rate (mV $s^{-1}$ )	electrolyte	capacitance (F g <sup>-1</sup> )	reference
MIL-100		5	0.1 M Na <sub>2</sub> SO <sub>4</sub>	44	63
MIL-101(Cr) derived Cr <sub>2</sub> O <sub>3</sub>	438	2	6 М КОН	180	64
Co-MOF	9.09	10		66	65
Co-NDC	20.29			73	66
Co-MOF	2900		1 M LiOH	103	67
UIO-66(Zr)	596	5	6 М КОН	104	68
Co-BDC derived Co <sub>3</sub> O <sub>4</sub>	47.12		2 M KOH	69	69
Mn-TCN MOF	8.65	5	1 M KOH	72	this work

double-layer capacitance and diffusion-limited transport, respectively. In addition, the circuit includes a charge-transfer resistance  $(R_{ct})$  that represents the rate at which electrons are transferred across the electrode-electrolyte interface. The internal resistance of the system  $(R_s)$  is comprised of the ionic resistance of the electrolyte, the intrinsic resistance of the active material, and the contact resistance at the interface between the active material and the current collector. 61 The existence of the constant phase element (CPE<sub>1</sub>) in the circuit is characteristic of a nonideal capacitor behavior, which is often utilized to account for the system behavior resulting from surface disorders, electrode porosity, and adsorption processes. 62 The probable cause for this disordered surface geometry of the electrode with a wide distribution of pore sizes is believed to be the formation of electrodes by random stacks of exfoliated MOF nanosheets.<sup>36</sup> The occurrence of the Warburg impedance (Z<sub>W</sub>), which we denote here as an additional constant phase element (CPE2), could be ascribed to a minor portion of the overall capacitance resulting from a pseudocapacitance mechanism, such as ion adsorption onto the electrode. 54,62 The impedance spectra were fitted by using ZSimpWin Software, and fitted parameters are summarized in Table 1. It is noteworthy that the number n signifies some details about the capacitive behavior taking place at the electrodes. A value of n = 1 indicates the ideal capacitor behavior, and it reflects the purity of the capacitive behavior. Considerably larger n values for the exfoliated sample compared to those of the bulk crystals may be connected to the increased surface accessibility of charge carrier ions in the KOH-based devices.

Table 2 illustrates a comparative view of the capacitive performance of some similar classes of MOF-based electrodes for supercapacitor applications.

### CONCLUSIONS

A tetracyanonickelate-based metal—organic framework (MOF) was successfully exfoliated using 1-dodecyl 2-pyrollidone (DDP) as the intercalant through a thermally assisted liquid-phase exfoliation technique. DDP can help increase the interlayer spacing of MOFs, making it easier to separate the layers and obtain individual nanosheets. In addition, it also stabilizes the exfoliated nanosheets in solution and prevents them from reaggregating. A large increase in the electroactive surface area from 0.69 m $^2$  g $^{-1}$  in bulk to about 8.65 m $^2$  g $^{-1}$  was

obtained in the exfoliated nanosheets. A thorough characterization of the samples before and after exfoliation was performed, which clearly showed for the exfoliated phase an increased band gap in the UV-vis spectra and a change in the peak shape along with a blue shift in the vibrational frequency in the Raman spectra. The two-dimensional feature of the nanosheets was revealed by SEM, AFM, and TEM images. The AFM statistical distribution shows that 50% of the nanosheets have a 1-4-layered morphology. A single-layer exfoliated nanoflake has an average dimension of  $20 \times 12 \text{ nm}^2$  and a thickness of ~1.2 nm. The HRTEM image and SAED pattern confirmed the presence of single- to few-layer nanosheets and that the crystallinity of the material remains intact after exfoliation. In this study, we demonstrated for the first time the effect of exfoliation on the electrochemical behavior of tetracyanonickelate-based MOFs. A comparison of the electrochemical properties in an aqueous (KOH) electrolyte solution revealed that the charge storage capacity of two-dimensional (2D) layered nanosheets obtained through exfoliation was significantly higher than those of their bulk counterparts. The Galvanostatic charge-discharge (GCD) test also reveals an increased specific capacitance from 18 F g<sup>-1</sup> in the bulk phase to 45 F g<sup>-1</sup> in the exfoliated phase. The cyclic stability test in bulk crystals demonstrates a growing capacitance retention of 125% over 1000 cycles of charge-discharge due to their further electrochemical exfoliation, but the exfoliated phase shows a maximum increase of 108% over 400 cycles before remaining stable for additional cycles. A 6-fold improvement in the values of specific capacitance obtained from CV measurement shows 13.0 F g<sup>-1</sup> in the bulk  $\rightarrow$  72.5 F g<sup>-1</sup> in the exfoliated phase at a scan rate of 5 mV s<sup>-1</sup>. The enhanced electrochemical performance is attributed to the increased surface area of the exfoliated nanosheets. This research presents an efficient technique for producing ultrathin Mn-TCN MOF nanosheets with superior capacitive performance. We believe that these electrochemically active 2D layer materials should benefit several electrochemical process-related applications from their large-scale production.

#### ASSOCIATED CONTENT

### Supporting Information

The Supporting Information is available free of charge at https://pubs.acs.org/doi/10.1021/acsami.3c14059.

Process flow of LPE, PXRD of the bulk and nanosheet, deconvoluted C 1s, N 1s, O 1s, Ni 2p, and Mn 2p XPS spectra; EDX mapping of the bulk crystal, additional AFM images and corresponding height profile of bulk and exfoliated samples; additional TEM images at low magnification and high resolution, CV curves in the nonfaradic region, and OCP measurement (PDF)

#### AUTHOR INFORMATION

#### **Corresponding Author**

Md Abdul Halim - Materials Science, Engineering, and Commercialization, Texas State University, San Marcos, Texas 78666, United States; o orcid.org/0000-0002-7214-923X; Phone: +1 (512) 2103547; Email: m h745@ txstate.edu

#### Authors

Subrata Karmakar - Department of Electrical Engineering, Texas State University, San Marcos, Texas 78666, United States; orcid.org/0000-0001-7619-5877

Md Abdul Hamid – Department of Electrical Engineering, Texas State University, San Marcos, Texas 78666, United

Chironjib Singha Samanta Chandan – Department of Biology, Texas State University, San Marcos, Texas 78666, United States

Imteaz Rahaman - Department of Electrical Engineering, Texas State University, San Marcos, Texas 78666, United

Michael E. Urena - Department of Chemistry and Biochemistry, Texas State University, San Marcos, Texas 78666, United States

Ariful Haque - Materials Science, Engineering, and Commercialization, Texas State University, San Marcos, Texas 78666, United States; Department of Electrical Engineering, Texas State University, San Marcos, Texas 78666, United States; o orcid.org/0000-0002-4285-9951

Maggie Yihong Chen - Materials Science, Engineering, and Commercialization, Texas State University, San Marcos, Texas 78666, United States; Department of Electrical Engineering, Texas State University, San Marcos, Texas 78666, United States

Christopher P. Rhodes - Materials Science, Engineering, and Commercialization, Texas State University, San Marcos, Texas 78666, United States; Department of Chemistry and Biochemistry, Texas State University, San Marcos, Texas 78666, United States; o orcid.org/0000-0003-4886-9875

Gary W. Beall - Materials Science, Engineering, and Commercialization, Texas State University, San Marcos, Texas 78666, United States; Department of Chemistry and Biochemistry, Texas State University, San Marcos, Texas 78666, United States

Complete contact information is available at: https://pubs.acs.org/10.1021/acsami.3c14059

The authors declare no competing financial interest.

#### ACKNOWLEDGMENTS

This study was partially supported by the Formosa Professorship Grant 4160081000 DF OCIR/Formosa from Dr. G.W.B. and the Office of Research and Sponsored Programs (ORSP) (ORSP-9000003094) from A.H. The authors are thankful to the Analysis Research Service Center (ARSC) facilities for material characterization and to the staff members of the Shared Research Operations (SRO) at Texas State University for their hands-on training and support. C.P.R. and M.E.U. acknowledge support from the NSF Partnerships for Research and Education in Materials (PREM) Center for Intelligent Materials Assembly (CIMA), Award No. 2122041.

## ABBREVIATIONS

Mn-TCN, manganese tetracyanonickelate MOF, metal-organic framework LPE, liquid-phase exfoliation DDP, 1-dodecyl-2-pyrrolidinone PC, pseudocapacitor CV, cyclic voltammetry GCD, galvanostatic charge-discharge EIS, electrochemical impedance spectroscopy ESR, equivalent series resistance CPE, constant phase element

#### REFERENCES

- (1) Wang, L.; Feng, X.; Ren, L.; Piao, Q.; Zhong, J.; Wang, Y.; Li, H.; Chen, Y.; Wang, B. Flexible Solid-State Supercapacitor Based on a Metal - Organic Framework Interwoven by Electrochemically-Deposited PANI. J. Am. Chem. Soc. 2015, 137, 4920-4923, DOI: 10.1021/jacs.5b01613.
- (2) Li, J. R.; Kuppler, R. J.; Zhou, H. C. Selective Gas Adsorption and Separation in Metal-Organic Frameworks. Chem. Soc. Rev. 2009, 38 (5), 1477-1504.
- (3) Lee, J.; Farha, O. K.; Roberts, J.; Scheidt, K. A.; Nguyen, S. T.; Hupp, J. T. Metal-Organic Framework Materials as Catalysts. Chem. Soc. Rev. 2009, 38 (5), 1450-1459.
- (4) Takashima, Y.; Martínez, V. M.; Furukawa, S.; Kondo, M.; Shimomura, S.; Uehara, H.; Nakahama, M.; Sugimoto, K.; Kitagawa, S. Molecular Decoding Using Luminescence from an Entangled Porous Framework. Nat. Commun. 2011, 2 (1), No. 168, DOI: 10.1038/ncomms1170.
- (5) Horcajada, P.; Chalati, T.; Serre, C.; Gillet, B.; Sebrie, C.; Baati, T.; Eubank, J. F.; Heurtaux, D.; Clayette, P.; Kreuz, C.; Chang, J. S.; Hwang, Y. K.; Marsaud, V.; Bories, P. N.; Cynober, L.; Gil, S.; Férey, G.; Couvreur, P.; Gref, R. Porous Metal-Organic-Framework Nanoscale Carriers as a Potential Platform for Drug Deliveryand Imaging. Nat. Mater. 2010, 9 (2), 172-178.
- (6) Wu, M.; Zhou, Z. Covalent Organic Frameworks as Electrode Materials for Rechargeable Metal-ion Batteries. Interdiscip. Mater. **2023**, 2 (2), 231–259.
- (7) Halim, A.; Karmakar, S.; Sourav, S.; Geerts, W. J.; Haque, A.; Beall, G. W. Crystallite Size-Dependent Magnetic Moment in Hydrogen Bridged Manganese Tetracyanonickelate Based Two-Dimensional Metal-Organic Frameworks. J. Magn. Magn. Mater. 2023, 571, No. 170573.
- (8) Rodríguez-Hernández, J.; Lemus-Santana, A. A.; Vargas, C. N.; Reguera, E. Three Structural Modifications in the Series of Layered Solids  $T(H\ 2O)\ 2[Ni(CN)\ 4]\cdot xH\ 2O$  with T=Mn, Co, Ni: Their Nature and Crystal Structures. C. R. Chim. 2012, 15 (4), 350-355.
- (9) Mak, K. F.; Lee, C.; Hone, J.; Shan, J.; Heinz, T. F. Atomically Thin MoS2: A New Direct-Gap Semiconductor. Phys. Rev. Lett. 2010, 105 (13), 2-5.
- (10) Kadantsev, E. S.; Hawrylak, P. Electronic Structure of a Single MoS 2 Monolayer. Solid State Commun. 2012, 152 (10), 909-913.
- (11) Wang, Y.; Yan, D.; El Hankari, S.; Zou, Y.; Wang, S. Recent Progress on Layered Double Hydroxides and Their Derivatives for Electrocatalytic Water Splitting. Adv. Sci. 2018, 5 (8), No. 1800064, DOI: 10.1002/advs.201800064.
- (12) Tan, C.; Cao, X.; Wu, X. J.; He, Q.; Yang, J.; Zhang, X.; Chen, J.; Zhao, W.; Han, S.; Nam, G. H.; Sindoro, M.; Zhang, H. Recent

- Advances in Ultrathin Two-Dimensional Nanomaterials. Chem. Rev. 2017, 117 (9), 6225–6331.
- (13) Zhang, W. Da.; Yan, X.; Li, T.; Liu, Y.; Fu, Q. T.; Gu, Z. G. Metal-Organic Layer Derived Metal Hydroxide Nanosheets for Highly Efficient Oxygen Evolution. *Chem. Commun.* **2019**, *55* (38), 5467–5470.
- (14) Chen, Z.; Forman, A. J.; Jaramillo, T. F. Bridging the Gap between Bulk and Nanostructured Photoelectrodes: The Impact of Surface States on the Electrocatalytic and Photoelectrochemical Properties of MoS2. *J. Phys. Chem. C* **2013**, *117* (19), 9713–9722.
- (15) Xiang, Q.; Yu, J.; Jaroniec, M. Synergetic Effect of MoS2 and Graphene as Cocatalysts for Enhanced Photocatalytic H2 Production Activity of TiO2 Nanoparticles. *J. Am. Chem. Soc.* **2012**, *134*, 6575–6578.
- (16) Chang, K.; Chen, W. Single-Layer MoS2/Graphene Dispersed in Amorphous Carbon: Towards High Electrochemical Performances in Rechargeable Lithium Ion Batteries. *J. Mater. Chem.* **2011**, *21* (43), 17175–17184.
- (17) Karmakar, S.; Boddhula, R.; Sahoo, B.; Raviteja, B.; Behera, D. Electrochemical Performance of Heterogeneous, Mesopores and Non-Centrosymmetric Core@shell NiCo2O4@MnO2 Nanocomposites and Its MWCNT Blended Complex for Supercapacitor Applications. J. Solid State Chem. 2019, 280, No. 121013.
- (18) Cao, L.; Yang, S.; Gao, W.; Liu, Z.; Gong, Y.; Ma, L.; Shi, G.; Lei, S.; Zhang, Y.; Zhang, S.; Vajtai, R.; Ajayan, P. M. Direct Laser-Patterned Micro-Supercapacitors from Paintable MoS2 Films. *Small* **2013**, 9 (17), 2905–2910.
- (19) Hao, G. P.; Tang, C.; Zhang, E.; Zhai, P.; Yin, J.; Zhu, W.; Zhang, Q.; Kaskel, S. Thermal Exfoliation of Layered Metal—Organic Frameworks into Ultrahydrophilic Graphene Stacks and Their Applications in Li–S Batteries. *Adv. Mater.* **2017**, *29* (37), 1702829.
- (20) Zhao, S.; Wang, Y.; Dong, J.; He, C. T.; Yin, H.; An, P.; Zhao, K.; Zhang, X.; Gao, C.; Zhang, L.; Lv, J.; Wang, J.; Zhang, J.; Khattak, A. M.; Khan, N. A.; Wei, Z.; Zhang, J.; Liu, S.; Zhao, H.; Tang, Z. Ultrathin Metal-Organic Framework Nanosheets for Electrocatalytic Oxygen Evolution. *Nat. Energy* **2016**, *1* (12), No. 16184, DOI: 10.1038/nenergy.2016.184.
- (21) Azad, M. A. K.; Rahman, M. H.; Nurani, S. J.; Halim, M. A.; Karim, M. A.; Gulshan, F. Rapid Decolorization of Acid Orange II in Aqueous Solution by Waste Iron Oxide Particles. *J. Mater. Environ. Sci.* **2016**, *7* (3), 685–693.
- (22) Sakaida, S.; Haraguchi, T.; Otsubo, K.; Sakata, O.; Fujiwara, A.; Kitagawa, H. Fabrication and Structural Characterization of an Ultrathin Film of a Two-Dimensional-Layered Metal-Organic Framework, {Fe(Py)2[Ni(CN)4]} (Py = Pyridine). *Inorg. Chem.* **2017**, *56* (14), 7606–7609.
- (23) Chen, R.; Huang, Y.; Xie, M.; Wang, Z.; Ye, Y.; Li, L.; Wu, F. Chemical Inhibition Method to Synthesize Highly Crystalline Prussian Blue Analogs for Sodium-Ion Battery Cathodes. *ACS Appl. Mater. Interfaces* **2016**, 8 (46), 31669–31676.
- (24) Zhang, K.; Varma, R. S.; Jang, H. W.; Choi, J. W.; Shokouhimehr, M. +Iron Hexacyanocobaltate Metal-Organic Framework: Highly Reversible and Stationary Electrode Material with Rich Borders for Lithium-Ion Batteries. *J. Alloys Compd.* **2019**, *791*, 911–917
- (25) Ren, W.; Qin, M.; Zhu, Z.; Yan, M.; Li, Q.; Zhang, L.; Liu, D.; Mai, L. Activation of Sodium Storage Sites in Prussian Blue Analogues via Surface Etching. *Nano Lett.* **2017**, *17* (8), 4713–4718.
- (26) Nie, P.; Yuan, J.; Wang, J.; Le, Z.; Xu, G.; Hao, L.; Pang, G.; Wu, Y.; Dou, H.; Yan, X.; Zhang, X. Prussian Blue Analogue with Fast Kinetics Through Electronic Coupling for Sodium Ion Batteries. *ACS Appl. Mater. Interfaces* **2017**, *9* (24), 20306–20312.
- (27) Fan, L.; Jia, C.; Zhu, Y. G.; Wang, Q. Redox Targeting of Prussian Blue: Toward Low-Cost and High Energy Density Redox Flow Battery and Solar Rechargeable Battery. *ACS Energy Lett.* **2017**, 2 (3), 615–621.
- (28) Wang, R. Y.; Shyam, B.; Stone, K. H.; Weker, J. N.; Pasta, M.; Lee, H. W.; Toney, M. F.; Cui, Y. Reversible Multivalent

- (Monovalent, Divalent, Trivalent) Ion Insertion in Open Framework Materials. *Adv. Energy Mater.* **2015**, 5 (12), 1401869.
- (29) Padigi, P.; Goncher, G.; Evans, D.; Solanki, R. Potassium Barium Hexacyanoferrate A Potential Cathode Material for Rechargeable Calcium Ion Batteries. *J. Power Sources* **2015**, 273, 460–464.
- (30) Tojo, T.; Sugiura, Y.; Inada, R.; Sakurai, Y. Reversible Calcium Ion Batteries Using a Dehydrated Prussian Blue Analogue Cathode. *Electrochim. Acta* **2016**, 207, 22–27.
- (31) Lee, J. H.; Ali, G.; Kim, D. H.; Chung, K. Y. Metal-Organic Framework Cathodes Based on a Vanadium Hexacyanoferrate Prussian Blue Analogue for High-Performance Aqueous Rechargeable Batteries. *Adv. Energy Mater.* **2017**, 7 (2), No. 1601491, DOI: 10.1002/aenm.201601491.
- (32) Deng, L.; Yang, Z.; Tan, L.; Zeng, L.; Zhu, Y.; Guo, L. Investigation of the Prussian Blue Analog Co3[Co(CN)6]2 as an Anode Material for Nonaqueous Potassium-Ion Batteries. *Adv. Mater.* **2018**, 30 (31), 1802510.
- (33) Baumann, A. E.; Burns, D. A.; Liu, B.; Thoi, V. S. Metal-Organic Framework Functionalization and Design Strategies for Advanced Electrochemical Energy Storage Devices. *Commun. Chem.* **2019**, 2 (1), 86.
- (34) Lee, J. S.; Nam, G.; Sun, J.; Higashi, S.; Lee, H. W.; Lee, S.; Chen, W.; Cui, Y.; Cho, J. Composites of a Prussian Blue Analogue and Gelatin-Derived Nitrogen-Doped Carbon-Supported Porous Spinel Oxides as Electrocatalysts for a Zn—Air Battery. *Adv. Energy Mater.* **2016**, 6 (22), No. 1601052, DOI: 10.1002/aenm.201601052.
- (35) Zhang, K.; Lee, T. H.; Bubach, B.; Ostadhassan, M.; Jang, H. W.; Choi, J. W.; Shokouhimehr, M. Layered Metal-Organic Framework Based on Tetracyanonickelate as a Cathode Material for: In Situ Li-Ion Storage. *RSC Adv.* **2019**, *9* (37), 21363–21370.
- (36) Winchester, A.; Ghosh, S.; Feng, S.; Elias, A. L.; Mallouk, T.; Terrones, M.; Talapatra, S. Electrochemical Characterization of Liquid Phase Exfoliated Two-Dimensional Layers of Molybdenum Disulfide. ACS Appl. Mater. Interfaces 2014, 6 (3), 2125–2130, DOI: 10.1021/am4051316.
- (37) Nash, T. L.; Beall, G. W.; Lee, B.; Higgins, C. Modeling, Characterization, and Exfoliation of a New Family of 2-D Materials. *Sci. Adv. Mater.* **2014**, *6* (4), 703–713.
- (38) Coleman, J. N.; Lotya, M.; O'Neill, A.; Bergin, S. D.; King, P. J.; Khan, U.; Young, K.; Gaucher, A.; De, S.; Smith, R. J.; Shvets, I. V.; Arora, S. K.; Stanton, G.; Kim, H. Y.; Lee, K.; Kim, G. T.; Duesberg, G. S.; Hallam, T.; Boland, J. J.; Wang, J. J.; Donegan, J. F.; Grunlan, J. C.; Moriarty, G.; Shmeliov, A.; Nicholls, R. J.; Perkins, J. M.; Grieveson, E. M.; Theuwissen, K.; McComb, D. W.; Nellist, P. D.; Nicolosi, V. Two-Dimensional Nanosheets Produced by Liquid Exfoliation of Layered Materials. *Science* 2011, 331 (6017), 568–571.
- (39) Shmeliov, A.; Shannon, M.; Wang, P.; Kim, J. S.; Okunishi, E.; Nellist, P. D.; Dolui, K.; Sanvito, S.; Nicolosi, V. Unusual Stacking Variations in Liquid-Phase Exfoliated Transition Metal Dichalcogenides. *ACS Nano* **2014**, *8* (4), 3690–3699.
- (40) Smith, R. J.; King, P. J.; Lotya, M.; Wirtz, C.; Khan, U.; De, S.; O'Neill, A.; Duesberg, G. S.; Grunlan, J. C.; Moriarty, G.; Chen, J.; Wang, J.; Minett, A. I.; Nicolosi, V.; Coleman, J. N. Large-Scale Exfoliation of Inorganic Layered Compounds in Aqueous Surfactant Solutions. *Adv. Mater.* **2011**, 23 (34), 3944–3948.
- (41) Yang, F.; Song, P.; Ruan, M.; Xu, W. Recent Progress in Two-Dimensional Nanomaterials: Synthesis, Engineering, and Applications. *FlatChem* **2019**, *18*, No. 100133.
- (42) Lemus-Santana, A. A.; Rodríguez-Hernández, J.; del Castillo, L. F.; Basterrechea, M.; Reguera, E. Unique Coordination of Pyrazine in T[Ni(CN)4]·2pyz with T = Mn, Zn, Cd. *J. Solid State Chem.* **2009**, 182 (4), 757–766.
- (43) Ahamed, T.; Rahaman, I.; Karmakar, S.; Halim, M. A.; Sarkar, P. K. Thickness Optimization and the Effect of Different Hole Transport Materials on Methylammonium Tin Iodide (CH 3 NH 3 SnI 3)-Based Perovskite Solar Cell. *Emergent Mater.* **2023**, *6*, 175.
- (44) Park, M.; Choi, J. S.; Yang, L.; Lee, H. Raman Spectra Shift of Few-Layer IV-VI 2D Materials. Sci. Rep. 2019, 9 (1), No. 19826.

- (45) Adilla, S. J.; Nurfani, E.; Kurniawan, R.; Satrya, C. D.; Darma, Y. Structural and Optical Properties Analysis of MoS2 Nanoflakes on Quartz Substrate as Prepared by Mechanical Exfoliation. *J. Phys.: Conf. Ser.* **2017**, 877 (1), No. 012036, DOI: 10.1088/1742-6596/877/1/012036.
- (46) He, X.; Lei, J.; Geng, Y.; Zhang, X.; Wu, M.; Zheng, M. Preparation of Microporous Activated Carbon and Its Electrochemical Performance for Electric Double Layer Capacitor. *J. Phys. Chem. Solids* **2009**, *70* (3–4), 738–744.
- (47) Zhang, W.; Huang, Z. H.; Cao, G.; Kang, F.; Yang, Y. A Novel Mesoporous Carbon with Straight Tunnel-like Pore Structure for High Rate Electrochemical Capacitors. *J. Power Sources* **2012**, 204, 230–235.
- (48) Xia, K.; Gao, Q.; Jiang, J.; Hu, J. Hierarchical Porous Carbons with Controlled Micropores and Mesopores for Supercapacitor Electrode Materials. *Carbon* **2008**, *46* (13), 1718–1726.
- (49) Fuertes, A. B.; Pico, F.; Rojo, J. M. Influence of Pore Structure on Electric Double-Layer Capacitance of Template Mesoporous Carbons. *J. Power Sources* **2004**, *133* (2), 329–336.
- (50) Portet, C.; Taberna, P. L.; Simon, P.; Flahaut, E. Influence of Carbon Nanotubes Addition on Carbon-Carbon Supercapacitor Performances in Organic Electrolyte. *J. Power Sources* **2005**, *139* (1–2), 371–378.
- (51) Liu, Y.; Wen, J.; Yao, H.; He, J.; Li, H. Enhancing the Corrosion Resistance Performance of Mg-1.8zn-1.74gd-0.5y-0.4zr Biomaterial via Solution Treatment Process. *Materials* **2020**, *13* (4), 836.
- (52) Zarach, Z.; Szkoda, M.; Trzciński, K.; Łapiński, M.; Trykowski, G.; Nowak, A. P. The Phenomenon of Increasing Capacitance Induced by 1T/2H-MoS2 Surface Modification with Pt Particles Influence on Composition and Energy Storage Mechanism. *Electrochim. Acta* **2022**, 435, No. 141389, DOI: 10.1016/j.electacta.2022.141389.
- (53) Bissett, M. A.; Kinloch, I. A.; Dryfe, R. A. W. Characterization of MoS2-Graphene Composites for High-Performance Coin Cell Supercapacitors. *ACS Appl. Mater. Interfaces* **2015**, *7* (31), 17388–17398.
- (54) Conway, B. E. Electrochemical Supercapacitors: Scientific Fundamentals and Technological Applications; Kluwer Academic/Plenum: Dordrecht, The Netherlands, 1999.
- (55) Kötz, R.; Hahn, M.; Gallay, R. Temperature Behavior and Impedance Fundamentals of Supercapacitors. *J. Power Sources* **2006**, 154 (2), 550–555.
- (56) Macdonald, J. R. Impedance Spectroscopy. Ann. Biomed. Eng. 1992, 20, 289-305.
- (57) Silva, T. A.; Zanin, H.; Saito, E.; Medeiros, R. A.; Vicentini, F. C.; Corat, E. J.; Fatibello-Filho, O. Electrochemical Behaviour of Vertically Aligned Carbon Nanotubes and Graphene Oxide Nanocomposite as Electrode Material. *Electrochim. Acta* **2014**, *119*, 114–119.
- (58) Sakharova, A.; Nyikost, L.; Pleskov, Y. Adsorption and Partial Charge Transfer at Diamond Electrodes-I. Phenomenology: An Impedance Study. *Electrochim. Acta* **1992**, *37* (5), 973–978.
- (59) Hernando, J.; Lud, S. Q.; Bruno, P.; Gruen, D. M.; Stutzmann, M.; Garrido, J. A. Electrochemical Impedance Spectroscopy of Oxidized and Hydrogen-Terminated Nitrogen-Induced Conductive Ultrananocrystalline Diamond. *Electrochim. Acta* **2009**, *54* (6), 1909–1915.
- (60) Prabaharan, S. R. S.; Vimala, R.; Zainal, Z. Nanostructured Mesoporous Carbon as Electrodes for Supercapacitors. *J. Power Sources* **2006**, *161* (1), 730–736.
- (61) Bo, Z.; Wen, Z.; Kim, H.; Lu, G.; Yu, K.; Chen, J. One-Step Fabrication and Capacitive Behavior of Electrochemical Double Layer Capacitor Electrodes Using Vertically-Oriented Graphene Directly Grown on Metal. *Carbon* **2012**, *50* (12), 4379–4387.
- (62) Jorcin, J. B.; Orazem, M. E.; Pébère, N.; Tribollet, B. CPE Analysis by Local Electrochemical Impedance Spectroscopy. *Electrochim. Acta* **2006**, *51* (8–9), 1473–1479.

- (63) Campagnol, N.; Romero-Vara, R.; Deleu, W.; Stappers, L.; Binnemans, K.; De Vos, D. E.; Fransaer, J. A Hybrid Supercapacitor Based on Porous Carbon and the Metal-Organic Framework MIL-100(Fe). *ChemElectroChem* **2014**, *1* (7), 1182–1188.
- (64) Ullah, S.; Khan, I. A.; Choucair, M.; Badshah, A.; Khan, I.; Nadeem, M. A. A Novel Cr2O3-Carbon Composite as a High Performance Pseudo-Capacitor Electrode Material. *Electrochim. Acta* **2015**, *171*, 142–149.
- (65) Lee, D. Y.; Shinde, D. V.; Kim, E. K.; Lee, W.; Oh, I. W.; Shrestha, N. K.; Lee, J. K.; Han, S. H. Erratum: Supercapacitive Property of Metal-Organic-Frameworks with Different Pore Dimensions and Morphology (Micropor. Mesopor. Mater. (2013) 171 (1) (53–57)). Microporous Mesoporous Mater. 2014, 186, 29.
- (66) Lee, D. Y.; Yoon, S. J.; Shrestha, N. K.; Lee, S. H.; Ahn, H.; Han, S. H. Unusual Energy Storage and Charge Retention in Co-Based Metal-Organic-Frameworks. *Microporous Mesoporous Mater.* **2012**, *153*, 163–165.
- (67) Díaz, R.; Orcajo, M. G.; Botas, J. A.; Calleja, G.; Palma, J. Cos-MOF-5 as Electrode for Supercapacitors. *Mater. Lett.* **2012**, 68, 126–128
- (68) Tan, Y.; Zhang, W.; Gao, Y.; Wu, J.; Tang, B. Facile Synthesis and Supercapacitive Properties of Zr-Metal Organic Frameworks (UiO-66). RSC Adv. 2015, 5 (23), 17601–17605.
- (69) Meng, F.; Fang, Z.; Li, Z.; Xu, W.; Wang, M.; Liu, Y.; Zhang, J.; Wang, W.; Zhao, D.; Guo, X. Porous Co3O4 Materials Prepared by Solid-State Thermolysis of a Novel Co-MOF Crystal and Their Superior Energy Storage Performances for Supercapacitors. *J. Mater. Chem. A* 2013, 1 (24), 7235–7241.